RESEARCH ARTICLE

WILEY **NMR** IN BIOMEDICINE

Unipolar MR elastography: Theory, numerical analysis and implementation

Christian Guenthner[1] ⓘ | Sweta Sethi[2] | Marian Troelstra[3,4] ⓘ |
Robbert J.H. van Gorkum[1] ⓘ | Mareike Gastl[1] ⓘ | Ralph Sinkus[3] ⓘ | Sebastian Kozerke[1] ⓘ

[1] Institute for Biomedical Engineering, University and ETH Zurich, Zurich, Switzerland

[2] Division of Research Oncology, Guy's and Saint Thomas' NHS Foundation Trust, London, UK

[3] Division for Imaging Sciences & Biomedical Engineering, King's College London, London, UK

[4] Department of Radiology and Nuclear Medicine, University Medical Center Amsterdam, Amsterdam, The Netherlands

Correspondence
Christian Guenthner, VOA B13, Voltastrasse 18, 8092, Zurich, Switzerland.
Email: guenthner@biomed.ee.ethz.ch

Funding information
European Union's Horizon 2020 research and innovation programme, Grant/Award Number: 668039; King's College London and University Medical Center Amsterdam

In MR elastography (MRE), zeroth moment balanced motion-encoding gradients (MEGs) are incorporated into MRI sequences to induce a phase shift proportional to the local displacement caused by external actuation. To maximize the signal-to-noise ratio (SNR), fractional encoding is employed, i.e., the MEG duration is reduced below the wave period. Here, gradients encode primarily the velocity of the motion-reducing encoding efficiency. Thus, in GRE-MRE, T_2^* decay and motion sensitivity have to be balanced, imposing a lower limit on repetition times (TRs).

We propose to use a single trapezoidal gradient, a "unipolar gradient", to directly encode spin displacement. Such gradients cannot be used in conventional sequences as they exhibit a large zeroth moment and dephase magnetization. By time-reversing a spoiled SSFP sequence, the spoiling gradient becomes an efficient unipolar MEG. The proposed "unipolar MRE" technique benefits from this approach in three ways: first, displacement encoding is split over multiple TRs increasing motion sensitivity; second, spoiler and MEG coincide, allowing a reduction in TR; third, motion sensitivity of a typical unipolar lobe is of an order of magnitude higher than a bipolar MEG of equal duration.

In this work, motion encoding using unipolar MRE is analyzed using the extended phase graph (EPG) formalism with a periodic motion propagator. As an approximation, the two-transverse TR approximation for diffusion-weighted SSFP is extended to incorporate cyclic motion. A complex encoding efficiency metric is introduced to

compare the displacement fields of unipolar and conventional GRE-MRE sequences in both magnitude and phase. The derived theoretical encoding equations are used to characterize the proposed sequence using an extensive parameter study. Unipolar MRE is validated against conventional GRE-MRE in a phantom study showing excellent agreement between measured displacement fields. In addition, unipolar MRE yields significantly increased octahedral shear strain-SNR relative to conventional GRE-MRE and allows for the recovery of high stiffness inclusions, where conventional GRE-MRE fails.

KEYWORDS

diffusion-weighted imaging, MR elastography, sampling strategies

1 | INTRODUCTION

Magnetic resonance elastography (MRE) allows the in vivo determination of the local tissue shear stiffness by time-resolved measurement of the 3D displacement field induced by an external actuator.[1] MRE utilizes the principle of phase contrast to encode the cyclic spin motion in the image phase.[2] Here, zeroth moment balanced gradients, ie, motion-encoding gradients (MEGs), are introduced before the readout to sensitize the image phase to displacements of the magnetization occurring while the gradient is switched on. Most MRE experiments currently rely on either spin echo (SE) or gradient-recalled echo (GRE) sequences.[1,3,4] Here, SE-based MRE benefits from the long echo time (TE) that allows maximization of the accumulated phase through matching of the MEG period to the wave period. Optimal motion sensitization with multiple gradient lobes and placement of MEGs before and after the echo pulse is possible.[4] However, fast readout strategies including echo-planar imaging (EPI) or spiral imaging need to be employed at the cost of T_2^* or frequency offset-related spatial blurring, eddy current-induced ghosting, or B0-inhomogeniety-induced geometric distortions.[5] In GRE-based MRE, a short Cartesian readout can be used due to the much shorter repetition time (TR). However, the need for a shorter MEG and reduced SNR loss due to T_2^* decay has to be addressed, which leads to the use of fractional encoding, where the duration of the MEG is shorter than the wave period.[6-8] In addition, the loss of longitudinal magnetization due to the short TR as well as the use of RF-spoiling to reduce spin-history effects leads to additional reduction in SNR.[9,10] Recent developments in MRE have been driven by the shortcomings of the SE- and GRE-based sequence concepts and have focused on new transducers,[11] sequence timing,[7,12] encoding schemes,[13] encoding approaches,[14-17] as well as excitation and readout schemes.[15,18-20]

Instead of spoiling magnetization after the readout, refocusing gradients can be used to effectively reuse transverse magnetization in subsequent repetition periods. This balanced steady-state free precession (bSSFP) approach has been exploited for MRE, which greatly benefits from its high SNR.[6,21,22] However, the continuous refocusing of transverse magnetization in bSSFP is dependent on phase accrual during the TR interval, which leads to the typical banding artifacts in the presence of off-resonance. In the context of MRE, the interference of motion phase and inhomogeneity leads to nonlinearity in the encoding of the vibratory motion, rendering bSSFP-based MRE difficult for in vivo applications.[6,21,22] Nonetheless, bSSFP-based MRE has been reported for hepatic and cardiac MRE.[6,23]

In addition to spoiled and balanced SSFP sequences, a generalized type of GRE sequence has recently regained interest for rapid relaxometry and diffusion-weighted SSFP (DW-SSFP) imaging.[24-27] These methods exploit additional refocusing gradients with integer multiples of the spoiling area before the readout of a conventional GRE sequence with consecutive balancing after the readout to refocus previously spoiled magnetization states while keeping the total spoiling area constant. These spoiling states, termed "configuration states", are carried over to the next TR period, where the subsequent RF pulse then partly flips the magnetization back to the longitudinal axis (storage), leaves it unaffected (dephasing configuration), or inverts it (rephasing configuration).[28] This leads to a plethora of discrete dephasing and rephasing configuration states, which can be refocused by a gradient that counteracts their accumulated spoiling.

This work proposes a new MRE sequence, which is based on the readout of the SSFP SE using a time-reversed spoiled SSFP sequence.[29] Here, the spoiling gradient acts as a highly efficient MEG, which allows considerable reduction in TRs as well as encoding fractions. In addition, 3D slab encoding leads to increased SNR compared with conventional consecutive or interleaved multi-slice (MS) acquisitions.[30] In contrast to conventional GRE- or SE-based MRE sequences, which can be solely understood on the basis of phase contrast, the proposed technique depends on spin history effects and necessitates the analysis of echo pathways and their motion sensitivities. The objective of this work is 5-fold: first, a qualitative theoretical understanding of echo formation and motion encoding in unipolar MRE is provided; second, a periodic motion propagator in the presence of gradient fields is derived for the extended phase graph (EPG) formalism, which allows for the numerical, quantitative analysis of the motion encoding in unipolar MRE using EPGs; third, a complex encoding efficiency is proposed, which takes phase differences in encoding into account

and hence allows direct comparison of the complex displacement field in both magnitude and phase of conventional and unipolar MRE despite their vast difference in encoding concept and sequence timing; fourth, a simplification of the full EPG-based simulation is attempted through adaptation of the two-transverse TR approximation, which was originally derived for DW-SSFP, allowing for fast encoding efficiency estimation[27,31]; and fifth, a comprehensive phantom study comparing unipolar MRE and conventional GRE-MRE is provided in order to demonstrate the feasibility of unipolar MRE and to validate theoretical findings.

2 | THEORY

In GRE-based MRE, a spoiling gradient is played after the readout of the free induction decay (FID) to dephase transverse magnetization (Figure 1A,C). We propose to read out the F_{-1} configuration state (SSFP-echo) instead, which is refocused by time-reversing the spoiled GRE sequence (Figure 1B), typically referred to as contrast-enhanced-FAST (CE-FAST), PSIF (Siemens; reversed FISP) or T2-CE-FFE (Philips).[34,35]
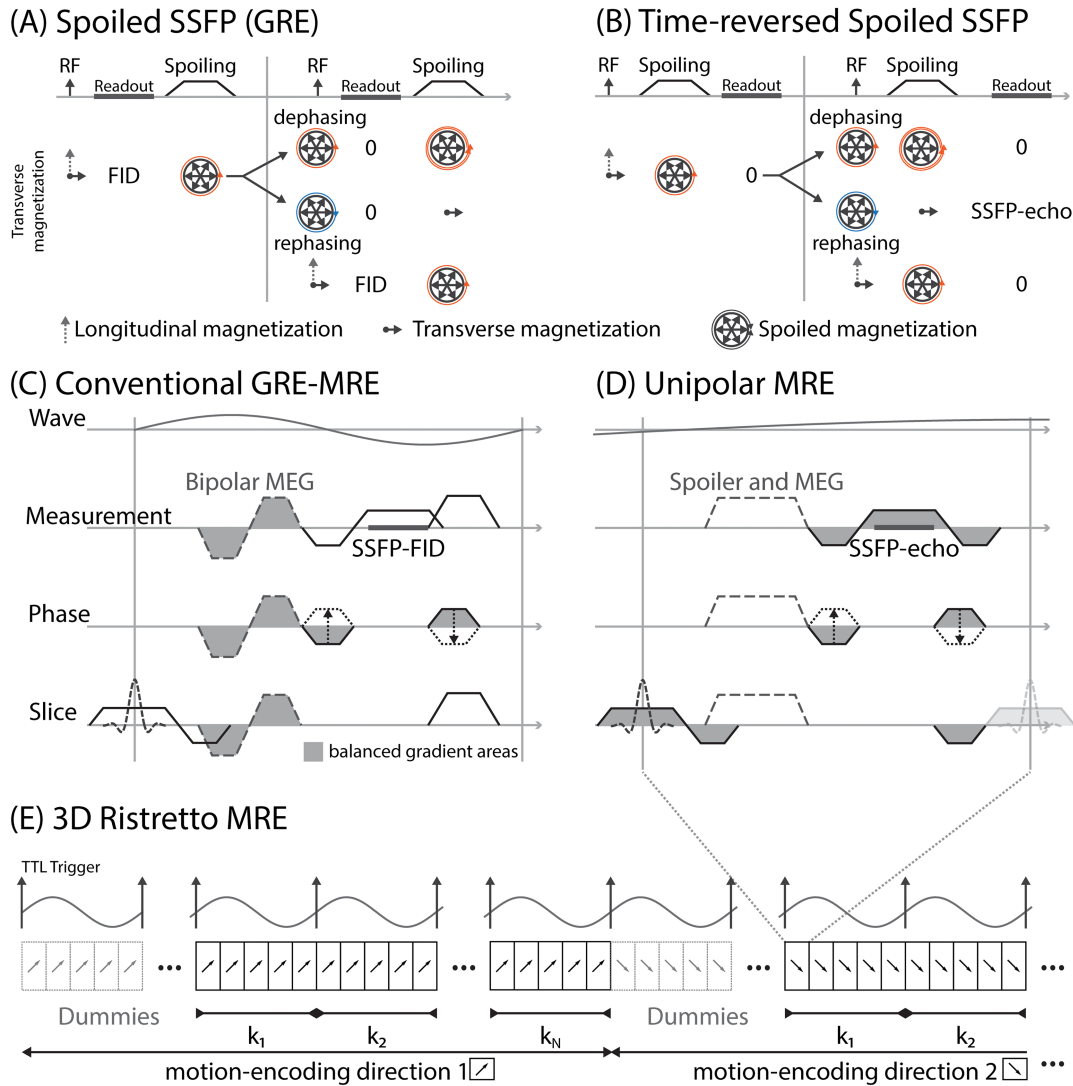
FIGURE 1 Depiction of echo formation in (A) spoiled (GRE) and (B) time-reversed spoiled SSFP. While the readout in spoiled GRE sequences is dominated by the FID, the first readout in time-reversed SSFP does not acquire any signal as the gradient spoils the signal of the FID. The second RF pulse splits the magnetization into a rephasing and a dephasing contribution. The former is refocused by the spoiling gradient and leads to the formation of the SSFP-echo (figure adapted from Scheffler, Ref. 32). Comparison of (C) conventional GRE-MRE with fractional bipolar motion-encoding gradients (MEGs) and (D) the proposed unipolar MRE sequence that uses the spoiling gradient as the MEG and reads out the SSFP-echo instead. The gray-shaded gradients are zeroth-moment balanced over one TR period. In (E), the global sequence timing of unipolar MRE is shown, which follows the 3D Ristretto scheme.[12,33] The innermost squares denote acquisitions according to (D), which are wave-phase interleaved (N_P = 5, N_D = 1). After a set of dummy shots to reach steady-state, successive k-lines are acquired in both slice- and phase-encoding direction (3D, slab excitation). After the full volume is acquired, the encoding direction is changed according to the Hadamard encoding scheme. A combination of TTL triggers and a correct choice of TR is used to ensure synchronization of the external wave generator and the unipolar MRE sequence

Contrary to conventional GRE sequences, the readout in the first TR period does not acquire any signal, as the spoiling gradient fully dephases the transverse magnetization. The second RF pulse partly leaves the transverse magnetization unaffected (0° component, dephasing configuration) and partly inverts it (180° component, rephasing configuration). The latter is refocused by the spoiling gradient and forms the SSFP-echo.[32] Since the spoiling gradient is played before the readout, the sequence becomes highly motion-sensitive, which is typically regarded as a drawback of time-reversed spoiled SSFP.[24,25,27,36-40] Here, this increased motion sensitivity is used for highly efficient elastography acquisitions. Since the bipolar MEG is replaced by a single gradient lobe, we will refer to the sequence as unipolar MRE.

In order to acquire N_P wave-phase offsets (with $N_P{\geq}2$) to extract amplitude and phase of the displacement field, the sequence timing follows the Ristretto MRE scheme[33] for 3D encoding (Figure 1E). Contrary to conventional 3D GRE-MRE schemes,[41] Ristretto interleaves the wave-phase acquisition allowing minimization of the TR. The wave phases are acquired in an interleaved fashion in the innermost sequence loop. The repetition time is constant and given by

$$T_R = \frac{N_D}{fN_P},$$

(1)

with N_D being a co-prime of N_P ($\gcd(N_D, N_P) = 1$). Each successive repetition is thus offset relative to the transistor-transistor logic (TTL) trigger played every N_P repetitions, where the wave phase offsets amount to

$$\phi_n = n\frac{2\pi N_D}{N_P}, \quad \text{with} \quad n = 0...N_P-1.$$

(2)

Since RF pulse and net dephasing from imaging gradients is equal in each TR and the underlying motion is periodic in $N_P T_R$, a steady-state of N_P distinct echoes forms.[42]

In the proposed sequence, the unipolar gradients for spoiling and motion sensitization coincide, necessitating the switching of the spoiling direction during sequence acquisition. To correct for phase contributions from imaging gradients, which are independent of the encoding direction, a reference phase image without motion sensitization is typically acquired in GRE-MRE.[7,8] However, since motion sensitization and spoiling is facilitated with the same gradient, an encoding scheme that encodes with equal total gradient moment for all encoding directions needs to be employed to ensure equal image contrast as well as sufficient spoiling. To this end, Hadamard encoding is incorporated, which encodes along the four diagonals of a regular cube.[8,43] The gradient direction matrix is given by

$$\hat{E} = \begin{bmatrix} +1 & +1 & -1 & -1 \\ +1 & -1 & +1 & -1 \\ +1 & -1 & -1 & +1 \end{bmatrix},$$

(3)

where the rows correspond to the three orthogonal gradient axes, while the columns denote successive encoding directions. Since the Hadamard scheme exhibits identical gradient moments in each of the three orthogonal gradient axes, isotropic image resolution is required to fulfill the gradient spoiling condition[30 (p. 353)]

$$\Delta k = \frac{2\pi}{\Delta x}n, \quad \text{with} \quad n \in \mathbb{N}^+$$

(4)

for each spatial dimension separately. To ensure proper spoiling of the SSFP signal, the spoiling direction is changed only after the full k-space for all wave phase offsets has been acquired and additional dummy shots are played for each encoding direction separately to reestablish the steady-state (see Figure 1E).

2.1 | Lowest order encoding efficiency of unipolar MRE: SSFP spin-echo contribution

In phase contrast-based MRE, the phase accrual φ in each voxel due to the periodic motion is proportional to the time-varying displacement field

$$\vec{r}(t) = \text{Im}\left\{\vec{d}\,e^{i\omega t}\right\}.$$

(5)

Here, $\vec{d} = \vec{r}_0 e^{i\phi}$ is the complex displacement amplitude, $\text{Im}\{\cdot\}$ the imaginary part, and $\omega = 2\pi f$ the angular wave frequency. The proportionality factor is denoted by the encoding efficiency ϵ of the gradient waveform, which is given by[3]

$$\epsilon = \gamma \int_{-\infty}^{\infty} d\tau\, G(\tau)e^{i\omega\tau},$$

(6)

where γ is the gyromagnetic ratio and $G(\tau)$ denotes the gradient waveform. While the phase of the complex encoding efficiency can often be neglected in conventional MRE, we specifically account for it to allow for absolute displacement field comparisons of conventional and unipolar MRE.

The sampling of the N_P equidistant phase offsets along the m-th direction can be stated as

$$\varphi_{n,m} = \text{Im}\left\{\epsilon\,\hat{E}^{\mathsf{T}}_{\bullet,m}\,\vec{d}\;e^{i2\pi/N_P n}\right\} + \varphi_{0,n}, \tag{7}$$

where $\varphi_{0,n}$ accounts for the phase accumulated by imaging gradients and the notation $\hat{E}_{\bullet,m}$ denotes the mth gradient direction. Thus the projection of the estimated displacement $\vec{d}$ including imaging gradient bias along the mth encoding direction is obtained by inverse discrete Fourier transformation

$$\hat{E}^{\mathsf{T}}_{\bullet,m}\vec{d} = \epsilon^{-1}\frac{2i}{N_P}\sum_{n=0}^{N_P-1}\varphi_{n,m}e^{-i2\pi/N_P n}, \tag{8}$$

which can then be solved for the unbiased $\vec{d}$ using the pseudo-inverse of the encoding matrix.[8]

2.1.1 | Bipolar MEG

The complex encoding efficiency for a bipolar MEG (Figure 2A), with duration $T = f^{-1}_{MEG}$, gradient strength G, and slope time t_d played at T_0 relative to the TTL-trigger is given by

$$\epsilon_{Bipolar} = -\frac{8i\gamma Ge^{i\omega(T/2+T_0)}}{t_d\omega^2}\sin\left(\frac{t_d\omega}{2}\right)\sin\left(\frac{T\omega}{4}\right)\sin\left(\frac{(T-2t_d)\omega}{4}\right). \tag{9}$$
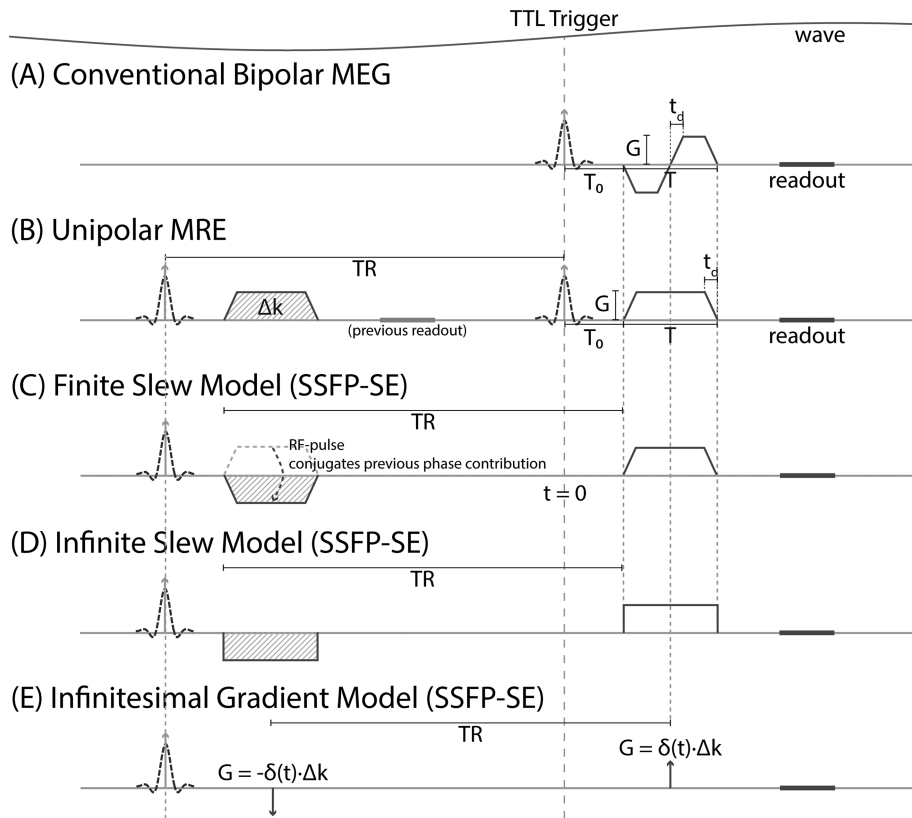
FIGURE 2 Timing graphs for (A) conventional GRE-MRE, (B) unipolar MRE, as well as the equivalent phase-contrast sequences (C)-(E) of unipolar MRE, where the first unipolar MEG is flipped to account for the complex conjugation of the echo signal through the second RF pulse. The phase-contrast model is equivalent to the lowest order echo pathway contributing to the unipolar MRE signal, which we term the "SSFP-SE" here. For comparability of the acquired displacement fields, absolute timing of the MEGs needs to be taken into account, where T_0 is the time offset between MEG and transistor-transistor logic (TTL) trigger, T is the total duration of the MEG, t_d is the gradient slope time and TR is the repetition time. The reference time-point to which the displacement field is calculated is set to coincide with the second RF pulse for unipolar MRE and the RF-pulse in conventional MRE, respectively. Approximations in (D) finite slew and (E) infinitesimal gradients are included in the analysis for better understanding of the encoding principle of unipolar MRE

2.1.2 | Infinite-slew unipolar MRE

The encoding efficiency of a single unipolar lobe (Figure 2D) with constant gradient strength G, infinite slew, and finite duration T can be obtained by solving Equation 6 and can be written as

$$\epsilon_{single\ lobe} = \Delta k\ \text{sinc}(q) e^{i\pi q + i\omega T_0},\tag{10}$$

where $q = Tf$ denotes the encoding fraction,[6] $\Delta k = \gamma G T$ is the gradient area of the unipolar lobe, and $\text{sinc}(x) = \sin(\pi x)/\pi x$ is the sinc-function.

The primary contribution to the SSFP-echo is given by the spin echo (SSFP-SE) of two successive TR periods, which is sensitized to motion twice (Figure 2B). The part of transverse magnetization, which is refocused, is complex conjugated at the time of the second RF pulse (Figure 2B). Thus, the motion sensitization of the first unipolar gradient is effectively inverted (Figure 2C). To obtain the correct encoding phase, the reference time with respect to the TTL trigger is set to be equal to the second RF pulse, thus the initial magnetization is excited at time $-T_R$. The lowest order approximation to the encoding efficiency of unipolar MRE assuming infinite slew is then given by

$$\epsilon = \epsilon_{single\ lobe} \cdot \left(\underbrace{-e^{-i\omega T_R}}_{Previous\ \text{TR}} + \underbrace{1}_{Current\ \text{TR}} \right) = 2i\,\Delta k\,\text{sinc}(q)\,\sin\left(\pi\frac{N_D}{N_P}\right) e^{i\pi\left(q - N_D N_P^{-1}\right) + i\omega T_0},\tag{11}$$

where the timing of the Ristretto scheme as specified in Equation 1 is implied. In the limit of an infinitesimal encoding gradient with finite moment Δk (Figure 2E), the encoding efficiency does not vanish but approaches

$$\lim_{q\to 0}\epsilon = 2i\Delta k\,\sin\left(\pi\frac{N_D}{N_P}\right) e^{-i\pi N_D N_P^{-1} + i\omega T_0}.\tag{12}$$

2.1.3 | Finite-slew unipolar MRE

Generalization of the previous infinite-slew model to the real situation of a trapezoidal gradient lobe with finite slope time t_d (Figure 2C) leads to

$$\epsilon_{Unipolar} = 2i\Delta k\cdot \text{sinc}(q_d)\,\text{sinc}(q - q_d)\,\sin\left(\pi\frac{N_D}{N_P}\right) e^{i\pi\left(q - N_D N_P^{-1}\right) + i\omega T_0},\tag{13}$$

where $q_d = t_d f$ is the fraction of the wave period that is lost to the gradient slewing. Taking the limit $t_d \to 0$, the infinite-slew encoding efficiency Equation 11 is directly recovered. By replacing $T \to T/2$ and $T_R \to T/2$ as well as temporal shifting by $T_0 \to T/2$, the encoding efficiency of the bipolar MEG with finite slew is obtained.

The above encoding efficiency Equation 13 is only valid under the assumption that each received signal is solely given by the SSFP-SE contribution, which is excited and refocused by the current and previous RF pulses. However, since no recovery period is included in time-reversed spoiled SSFP sequences compared with conventional SE sequences and the sequence TR is usually much shorter than T_2, spin history effects need to be taken into account. These will affect the encoding efficiency by constructive and destructive interference.

2.2 | EPG formalism for unipolar MRE

In order to describe dephased magnetization states, EPG formalism is used. A comprehensive introduction to EPGs is given in the review article by Weigel,[28] which we follow here in terms of notation and conventions; and which should be consulted for explicit mathematical expressions of the operators. EPGs describe spoiled magnetization as a superposition of complex configuration states $F_\pm$ and Z. There, the central assumption is uniformity of space so that spatial dependencies in the magnetization distribution are solely arising due to gradient fields. Each configuration state corresponds to a Fourier component $\vec{k}$ of the transverse $M_\pm = M_x\left((\vec{r}), +iM_y(\vec{r})\right)$ and longitudinal $M_z(\vec{r})$ magnetization distribution. The formal definitions are

$$F_\pm(\vec{k}) = \int d^3 r \left(M_x(\vec{r}) \pm iM_y(\vec{r}) \right) e^{-i\vec{k}\cdot\vec{r}}, \text{ and}\tag{14}$$

$$Z(\vec{k}) = \int d^3 r\, M_z(\vec{r}) e^{-i\vec{k}\cdot\vec{r}}.\tag{15}$$

RF pulses, gradient fields, motion and relaxation are described in terms of operators acting on these configuration states. RF pulses $\mathbf{T}_\phi(\alpha)$ distribute magnetization between transverse and longitudinal configuration states independent of the spatial frequency $\vec{k}$, where α denotes the flip angle

and ϕ the pulse phase. Relaxation $\mathbf{E}_{T_1,T_2}$ leads to attenuation of transverse and longitudinal states and the recovery of longitudinal magnetization in the $k = 0$ configuration state only. Gradients $\mathbf{S}\left(\Delta \vec{k}\right)$ shift the population of transverse configuration states by the respective $\Delta \vec{k}$-value of the gradient. Finally, motion and diffusion can be incorporated via motion propagators $\mathbf{J}$, which are typically k-value dependent. Bulk motion leads to phase accrual (Fourier shift theorem) and random motion to attenuation (phase dispersion). A pulse sequence is described as a concatenation of these operators.

In Figure 3, EPGs for unipolar MRE in the presence and absence of periodic motion are shown. Since the spoiling area is constant for all imaging shots, the y-axis counts the spatial frequencies in units of the spoiling area Δk in the direction of the spoiling gradient. The unipolar spoiling gradient, which is played before the readout in the time-reversed spoiled SSFP sequence, leads to dephasing of configuration states with $k > 0$ and to respective rephasing of configurations with $k < 0$. Due to the presence of periodic motion, the configuration states accumulate a phase depending on their k-value. This is depicted by the bending of the configuration states, which is proportional to the relative phase accrual with respect to the previous RF pulse. This should not be confused by an actual change in spatial frequency of the respective states.

In addition to periodic motion, diffusion attenuates configuration states with high spatial frequency.[28] This is illustrated 2-fold: first, by reduced line thickness and opacity in the EPG with increasing $|k|$ and, second, by the diffusion attenuation plot to the right. At the bottom of the graph, the unipolar MRE sequence is denoted together with its simplified operator notation.

In the present work, two EPG-based analyses are proposed: (i) the EPG representation of unipolar MRE can be used for full numerical encoding efficiency calculations by driving a forward calculation according to the operator sequence denoted in Figure 3 to steady-state; and (ii) a reverse analysis of the echo signal contributions can be conducted, describing the lowest order perturbation theory solution of the EPG in terms of T_2-decay. This approach is commonly known as the two-transverse TR-approximation, which has been proposed before for the understanding of diffusion contrast in DW-SSFP sequences, and which is extended here to incorporate periodic motion.[31,44]
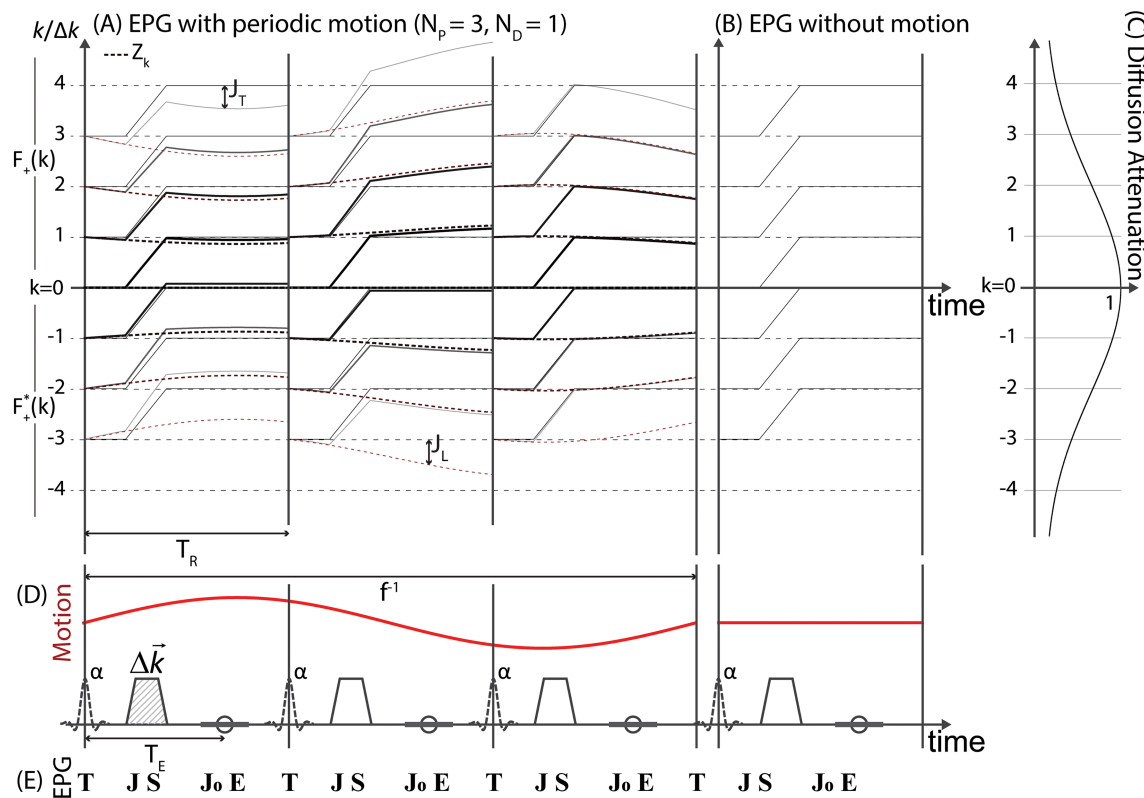
FIGURE 3   (A) Pictorial description of the extended phase graph in steady-state for the case of three encoded wave phases (N_P = 3) and a delay of one (N_D = 1). Solid lines denote transverse magnetization states, whereas broken lines depict longitudinal magnetization. The overlaid thin solid and dashed lines as well as the graph in (B) denote the EPG in the absence of motion. The unipolar MRE sequence is shown in abbreviated form in (D). The change in configuration state phase in the presence of periodic motion is depicted by the bending of the EPG. Here, the change in phase is depicted relative to the time of the RF pulse. Motion sensitivity of the configuration states increases linearly with $|k|$ resulting in nonlinear encoding of displacements if configuration states are mixed. The bending of the EPG is for visualization purposes only and should not be confused with a change in k. In (C), diffusion attenuation is shown, which attenuates high spatial frequency states. This is also depicted in the EPG by the lighter color of the graph. Diffusion and T_2-decay limit the mixing of different configuration states reducing overall sensitivity to relaxation and sequence parameters. (E) shows the shortened EPG propagator ordering, which can be used to simulate the steady-state magnetization

2.3 | Motion propagator for unipolar MRE

The motion propagator for coherent bulk motion $\vec{r}(t)$ subject to an arbitrary k-space trajectory $\vec{k}(t)$ is given by[28]

$$\mathbf{J}\left(\vec{k}(t), \vec{r}(t); t\right) = \exp\left\{-i\int_0^t d\tau\, \vec{k}(\tau) \cdot \frac{d\vec{r}(\tau)}{d\tau}\right\}, \tag{16}$$

with the usual definition of k

$$\vec{k}(t) = \gamma\int_0^t d\tau\, \vec{G}(\tau) + \vec{k}_0. \tag{17}$$

Here, $\vec{k}_0$ is the initial wave vector of the configuration state. Assuming periodic motion (Equation 5), the general motion propagator for a single constant gradient lobe with infinite slew and finite duration T is given by

$$\mathbf{J} = \exp\left\{-i\frac{\vec{r}_0 \cdot \Delta\vec{k}}{2\pi fT}(2\pi fT\sin(2\pi fT + \phi) + \cos(2\pi fT + \phi) - \cos(\phi))\right\}\mathbf{J}_0 \tag{18}$$

and

$$\mathbf{J}_0 = \exp\left\{-i\vec{r}_0 \cdot \vec{k}_0(\sin(2\pi fT + \phi) - \sin(\phi))\right\}, \tag{19}$$

where $\Delta\vec{k} = \gamma\vec{G}T$ is again the area of the gradient lobe. The propagator for longitudinal magnetization as well as transverse magnetization in the absence of a gradient field can be found by setting $\Delta\vec{k}$ to zero and is thus given by $\mathbf{J}_0$ only. Since a unipolar lobe causes a change in configuration state population, the full unipolar propagator is given by a concatenation of motion sensitization and subsequent shifting of the configuration state population according to the gradient operator $\mathbf{S}$. The motion propagator for the general case of a trapezoidal lobe with finite slew is stated in Appendix A (see the supporting information).

In addition to motion sensitization, the dephased magnetization states are subject to diffusion attenuation.[28] The 1D diffusion attenuation operator is given by

$$\mathbf{D}_{1D}(k(t), D, t) = \exp(-b_tD), \quad \text{with} \quad b_t := \int_0^t d\tau\, \left\|\vec{k}(\tau)\right\|^2. \tag{20}$$

Thus, for transverse magnetization in the case of an infinite-slew gradient lobe, the operator becomes

$$\mathbf{D} = \exp\{-DT\Delta k(k_0 + \Delta k/3)\}\mathbf{D}_0, \tag{21}$$

with

$$\mathbf{D}_0 = \exp\left\{-DTk_0^2\right\}. \tag{22}$$

Again, $\mathbf{D}_0$ is the propagator in the absence of the gradient as well as the corresponding propagator for longitudinal magnetization states. The diffusion attenuation can be incorporated in the general motion propagator for unipolar MRE by applying the replacement $\mathbf{J} \rightarrow \mathbf{JD}$ and $\mathbf{J}_0 \rightarrow \mathbf{J}_0\mathbf{D}_0$, respectively.

Diffusion attenuation is an important factor in unipolar MRE, as it leads to attenuation of high spatial frequency states since the exponential scales proportional to k^2. This ultimately reduces the sensitivity of the sequence to T_1 and T_2 relaxation, flip angle, as well as leading to the reduction of the nonlinearity of motion encoding.

2.4 | Extending the two-transverse TR approximation in the presence of periodic motion

The two-transverse TR approximation is an approximate solution to the problem of diffusion weighting in SSFP-based sequences.[31,44] It determines the signal based on the assumption that only echoes with no more than two transverse TR-periods contribute to the signal amplitude of the SSFP-echo. This corresponds to the lowest order Taylor series expansion of the analytical solution in $E_2 = \exp\{-T_R/T_2\}$.

In Figure 4, the EPG is drawn in reverse, ie, starting from an echo and tracing back the signal contributions in lowest order perturbation theory in E_2. This leads to the graphical depiction of the three distinct echo pathways of the two-transverse TR approximation. Solid paths are transverse
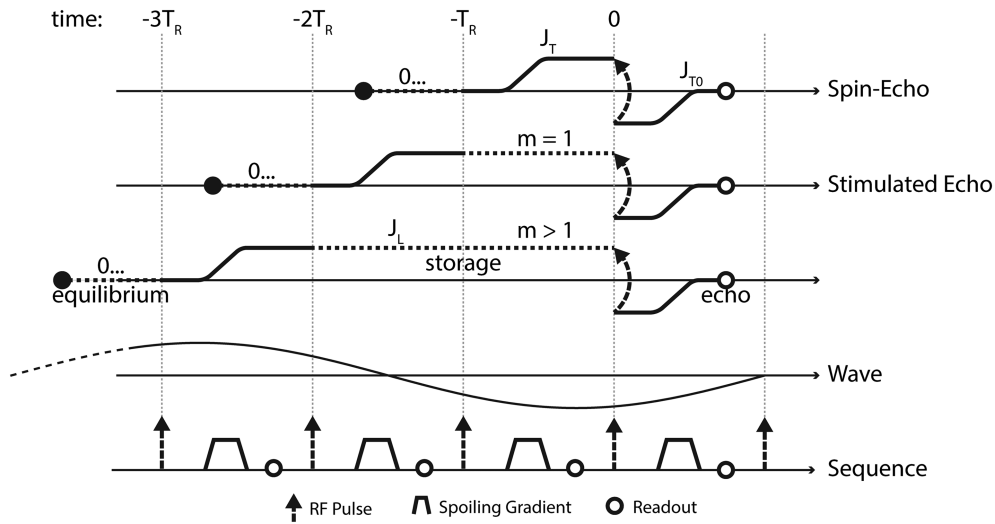
FIGURE 4 Pictorial description of the two-transverse TR approximation for $N_P = 5$ and $N_D = 1$ tracing back the origin of the echo. Equilibrium magnetization undergoes an infinite series of longitudinal storage periods before the first flip into the transverse plane. In the stimulated echo case, m > 0 longitudinal storage periods are assumed before flipping the magnetization back into the transverse plane, where it refocuses to form an echo. For m = 0, no longitudinal storage is found and the magnetization is directly flipped into its conjugate state forming the spin-echo of the spoiled SSFP sequence. The unipolar MRE sequence is depicted in the last row, where the arrows denote RF pulses, trapezoids represent the spoiling gradients and circles denote echo time-points

magnetization states, whereas dotted lines denote longitudinal magnetization. Each path is preceded by infinitely many longitudinal magnetization-only paths to account for the equilibrium magnetization. Thus, every pathway can be characterized by the number m of longitudinal storage periods. Transverse magnetization is subject to motion sensitization according to the transverse motion propagators $\mathbf{J}_T((m+1)T_R)$ and $\mathbf{J}_{T0}$. $\mathbf{J}_{T0}$ corresponds to the motion sensitization of the refocusing pathway before readout, while $\mathbf{J}_T((m+1)T_R)$ determines motion sensitization after excitation. Longitudinal storage in elevated configuration states (here, only Z_1 contributes) are modulated according to $\mathbf{J}_L(mT_R)$, respectively. The definition of the motion propagators follows from careful evaluation of Equation 18 under consideration of the number and timing of the transverse and longitudinal echo pathways. The respective terms are given in Appendix B (see the supporting information).

Under consideration of the periodicity of the motion propagators

$$\mathbf{J}_T((m+N_P)T_R) = \mathbf{J}_T(mT_R) \quad \text{and} \quad \mathbf{J}_L((m+N_P)T_R) = \mathbf{J}_L(mT_R) \tag{23}$$

the derivation of the two-transverse TR approximation can be carried out by following the derivation of McNab and Miller,[44] which is laid out explicitly in Appendix C (see the supporting information). In conclusion, the echo signal is given by

$$S = SE + STE_1 + \sum_{m=2}^{\infty} STE_m, \tag{24}$$

where the SE and STE contributions are found to be

$$SE = -\frac{M_0(1-E_1)E_2 \sin^2(\alpha/2)\sin(\alpha)}{1-E_1\cos(\alpha)} \cdot \mathbf{J}_T^*(T_R)\mathbf{J}_{T0}, \tag{25}$$

$$STE_1 = -\frac{M_0(1-E_1)E_1E_2\sin^3(\alpha)}{2(1-E_1\cos(\alpha))} \cdot \mathbf{J}_T^*(2T_R)\mathbf{J}_L^*(T_R)\mathbf{J}_{T0}, \quad \text{and} \tag{26}$$

$$\sum_{m=2}^{\infty} STE_m = -\frac{M_0(1-E_1)E_1^2E_2\sin^3(\alpha)\cos(\alpha)}{2(1-E_1\cos(\alpha))} \frac{\kappa(N_P)\mathbf{J}_{T0}}{1-(E_1\cos(\alpha))^{N_P}}, \tag{27}$$

with $E_{1/2} = \exp\{-T_R/T_{1/2}\}$ and

$$\kappa(N_P) = \sum_{n=0}^{N_P-1}(E_1\cos(\alpha))^n \cdot \mathbf{J}_T^*((n+3)T_R)\mathbf{J}_L^*((n+2)T_R). \tag{28}$$

The final step, determination of the motion phase accumulated in steady-state, is performed by Fourier transformation of the argument of the

complex steady-state signal (Equation 24) according to

$$\epsilon_f = r_0^{-1}\mathcal{F}(\arg(S)) = \frac{i}{\pi r_0}\int_0^{2\pi}d\phi\,\arg(S)e^{-i\phi}. \tag{29}$$

Here, the integration is normalized such that the Fourier transformation reproduces amplitude and phase of a sinusoidal oscillation according to

$$\mathcal{F}(a\sin(\phi+b)) = ae^{ib}. \tag{30}$$

To the knowledge of the authors, no closed-form solution of Equation 29 exists. Hence, the final solution is obtained numerically using MATLAB.

3 | METHODS

3.1 | EPG simulations

The EPG simulations were based on the Stanford EDU MATLAB implementation[45] and run in MATLAB 2018a (MathWorks, Natick, Massachusetts). The unipolar motion propagator was implemented according to Equation 16 including diffusion attenuation and using the full trapezoidal gradient waveform. The steady-state signal behavior was simulated by repeated application of the EPG formalism to drive an initial equilibrium magnetization configuration to steady-state. The propagator ordering is given in abbreviated form in Figure 3 and was evaluated using the appropriate timing constraints given by the Ristretto MRE scheme (Equation 1). The analytical two-transverse TR approximation model was numerically solved using MATLAB as well.

In order to determine the encoding efficiency in the steady-state, the unwrapped signal phase was obtained for the last N_P elements, which was then reordered according to Equation 2 and subsequently Fourier-transformed. The first Fourier component—corresponding to the actuation frequency—was divided by the input wave amplitude yielding the encoding efficiency. If not stated otherwise, all calculations were performed with the following set of parameters to be compliant with the phantom experiment: T_1/T_2 = 2400/190 ms, diffusion coefficient D = 1.7 x 10^{-3} mm^2/s, number of wave phases N_P = 5, Ristretto delay parameter N_D = 1, wave frequency f = 35 Hz, gradient duration T = 2 ms (encoding fraction q = 7%), gradient strength G = 20.9 mT/m, gradient slope time t_d = 0.13 ms, displacement amplitude d = 10 μm and flip angle = 20°, resulting in a sequence TR of 5.71 ms. EPG simulations were run with a fixed number of 700 EPG states to account for spin history and were iterated to steady-state with 500 iterations of the phase loop corresponding to 500 x N_P = 2500 TR periods.

3.2 | Phantom comparison

Unipolar MRE as well as conventional GRE-MRE were performed on a gel phantom with four cylindrical inclusions (CIRS Inc., Norfolk, Virginia) using a 3 T Philips Ingenia system (Philips Healthcare, Best, the Netherlands). The signal was received using a 15-channel head coil, and 35 Hz electromagnetic actuation was employed.[4] The phantom was positioned upright in the head coil with the actuator placed on top with primary actuation being in the top-down direction. Slice selection direction was chosen anterior–posterior (see also Figure 8). In the following, scan parameters are stated in pairs of "conventional/unipolar MRE"; 20/10 repeat measurements were acquired to investigate the dependence of the shear stiffness estimates with increasing SNR. All measurements were performed using fractional encoding[6] with encoding fractions of 17.5%/7%, 11.9/20.9 mT/m bipolar/unipolar MEGs (duty cycle limitation in conventional MRE) resulting in an encoding efficiency of 4.01/10.8 rad/mm, 3 mm^3 isotropic resolution and 64 × 48 matrix size acquired using a 30°/20° flip angle, Cartesian readout, and third/first in-phase water-fat echo-time (TE 6.9/2.3 ms). Conventional GRE-MRE was performed as a MS acquisition of 12 interleaved slices resulting in a TR per slice of 110.7 ms, while unipolar MRE was performed using slab-excitation and phase encoding of 36 slices with a TR of 5.71 ms. The increased FOV in slice direction was chosen to eliminate fold-over artifacts due to production impurities with strong susceptibility mismatch in the bottom of the phantom. The conventional GRE-MRE sequence was accelerated using the Ristretto MRE[12,33] scheme acquiring eight wave-phase offsets in reverse order (N_D = 7) and excitation and readout of the 12 slices for one wave-phase offset within N_W = 3 wave periods. Only five wave-phase offsets were acquired with unipolar MRE to conform with sequence-timing constraints. The spoiling gradient was chosen to result in 5 × $2\pi/\Delta x$ phase accumulation along each spatial direction, separately. The acquisition of all wave-phase offsets and encoding directions for a single slice took 14.3/7.0 seconds, respectively. Synchronization to the external wave generator was achieved using a TTL trigger signal. In order to achieve a magnetization and wave steady-state, 62 dummy shots were used for unipolar MRE, totaling to 1.8 seconds per encoding direction (conventional MRE: 10 dummies, 1.1 seconds/encoding direction).

A second set of phantom scans was performed at 70 Hz actuation frequency. Unipolar MRE with five wave-phase offsets was acquired with N_D = 2 (36 slices), while conventional MRE was acquired with N_W = 7 and N_D = 3 (12 slices). Due to the shorter wavelength and thus better conditioned inversion at 70 Hz, 10 averages were acquired for both techniques. Remaining scan parameters were equivalent to the 35 Hz acquisition, leading to an encoding fraction of 35%/14%, an encoding efficiency of 7.5/10.2 rad/mm, and a scan duration of 13.6/7.0 seconds per slice and average, for conventional/unipolar MRE, respectively.

In addition to the acquisition of the MRE datasets, quantitative parameter mapping was performed to obtain local estimates for T_1, T_2, the apparent diffusion coefficient (ADC) and the fractional anisotropy (FA) of the phantom in one representative slice in order to calculate the local, complex encoding efficiency for the unipolar MRE acquisition. T_1 and T_2 estimates were obtained on the same 3 T Philips Ingenia system using a spoiled GRE-based MR fingerprinting (FISP-MRF)[46] sequence with a constant TR of 16 ms, fully sampled multi-shot spiral acquisition with 15 interleaves, a repetition delay of six seconds to ensure relaxation to equilibrium, and 1000 variable excitations after adiabatic inversion resulting in a total scan duration of 5.5 minutes. The flip angle train is given in Figure S1. Dictionary-based matching was performed to determine T_1 and T_2 locally using MATLAB 2018a (MathWorks). The dictionary was created based on the Stanford EDU MATLAB EPG implementation.[45] The dictionary resolution is given in Table S1.

SE-based diffusion tensor imaging (DTI) with unipolar encoding gradients, six encoding directions and five b-values (linearly interpolated, 0 to 1000 ms/mm^2) was performed to obtain an estimate of the ADC and FA in a single slice.[47,48] The scan was performed on a 1.5 T Philips Achieva system (Philips Healthcare). The signal was received using an eight-channel head coil. Sequence parameters were 3 x 3 mm^2 in-plane resolution, 8 mm slice thickness, 10 averages, single-shot EPI readout, matrix size 64 x 45, FOV 196 x 136, flip angle 90°/180°, 60 ms echo time, and a TR of 1000 ms, resulting in 4 minutes 11 seconds scan duration.

For comparability, the FOV of the unipolar MRE scan was cropped to the 12 central slices to match the conventional MRE scan prior to postprocessing. The image phase was spatially unwrapped using the statistical cost, network-flow algorithm for phase unwrapping (SNAPHU),[49-52] temporally aligned, and decoded using the pseudo-inverse of the encoding matrix.[8] Cumulative averaging of the decoded wave phase images was performed prior to Fourier-transformation. The complex displacement fields were estimated from the first Fourier component and corrected for the encoding efficiency of the conventional and unipolar MRE scans. The phase of the complex displacement field of the conventional MRE scans was corrected for inter-slice phase shifts according to the Ristretto MRE scheme.[12,33] The encoding efficiency of the unipolar MRE acquisitions was determined using the two-transverse TR approximation assuming homogenous relaxation and diffusion (T_1 = 2.4 s, T_2 = 190 ms and D = 1.7 x 10^{-3} mm^2/s). The complex displacement fields were then further processed without smoothing using a FEM-based reconstruction algorithm[53] to obtain the complex shear stiffness, where we report the averaged magnitude over the innermost six slices. In addition, the wave-phase images were used to estimate the displacement noise in each voxel, allowing for the determination of the octahedral shear strain-SNR (OSS-SNR).[54] OSS-SNR values are reported for the inclusions and for the background as ROI-averaged values.

4 | RESULTS

4.1 | EPG simulations

In Figure 5, the encoding efficiency of unipolar MRE is shown as a function of tissue parameters T_1, T_2, and the diffusion coefficient D within the phase-contrast approximation (red, SSFP-SE contribution), the two-transverse TR approximation (yellow), and the full EPG simulation (violet). If applicable, full EPG simulations neglecting diffusion attenuation are shown in dotted violet. Sequence parameters were held constant at the values displayed by the vertical dashed lines. In Figure 5A, the encoding efficiency is shown as a function of the diffusion coefficient. The phase-contrast model is independent of diffusion by construction. For typical diffusion coefficients in vivo (D = ~2 x 10^{-3} mm^2/s), the encoding efficiency obtained from full EPG simulations is within 3% of the two-transverse TR approximation and converges for strong diffusion. Neglecting diffusion, the encoding efficiency obtained from full EPG simulations deviates by ~20%.

In Figure 5B-D, the encoding efficiency is shown as a function of T_1 and T_2 under the assumption of finite diffusion (D = 1.7 x 10^{-3} mm^2/s). Figure 5B shows the case of long T_2 relaxation (190 ms), where full EPG and the two-transverse TR approximation show little dependency on T_1 with variations below 3%. Figure 5D shows the case of short T_2 relaxation (30 ms). For long T_1 (>1000 ms), full EPG with and without diffusion as well as the two-transverse TR approximation become equivalent. At very short T_1 (<100 ms), maximal deviations of up to 5% are found. Contrary to the long T_2 case, diffusion only plays a minor role, as shown by the near equivalence of full EPG with and without diffusion. This can also be appreciated in Figure 5C, which shows the T_2 dependency for the case of long T_1 (2400 ms). Below 50 ms, the two-transverse TR approximation and the full EPG with and without diffusion are closely aligned (<1% deviation). For increasing T_2, full EPG simulations, especially without diffusion attenuation, show decreasing encoding efficiency compared with the two-transverse TR approximation. Again, the encoding efficiency of both phase-contrast and the two-transverse TR approximation are independent of T_2 by design. The dependency of the encoding efficiency phase angle on the same set of parameters is shown in Figure S3.

In Figure 6, the encoding efficiency of unipolar MRE is compared for different sequence parameters. Figure 6A shows the encoding efficiency as a function of encoding fraction q and compares the different unipolar MRE approximations against conventional phase-contrast MRE with bipolar MEGs (blue). The red line indicates the encoding fraction limit imposed by the sequence timing (here N_P = 5, N_D = 1), which limits the duration of the encoding gradient. In the small q regime (<10%), the encoding efficiency of unipolar MRE is proportional to q, whereas conventional bipolar MRE is proportional to q^2. In Figure 6B, the dependency on the sequence-timing parameters N_P and N_D is shown. The SSFP-SE contribution shows its maximal encoding efficiency at N_P = 2, where the phase contributions from two consecutive TRs interfere
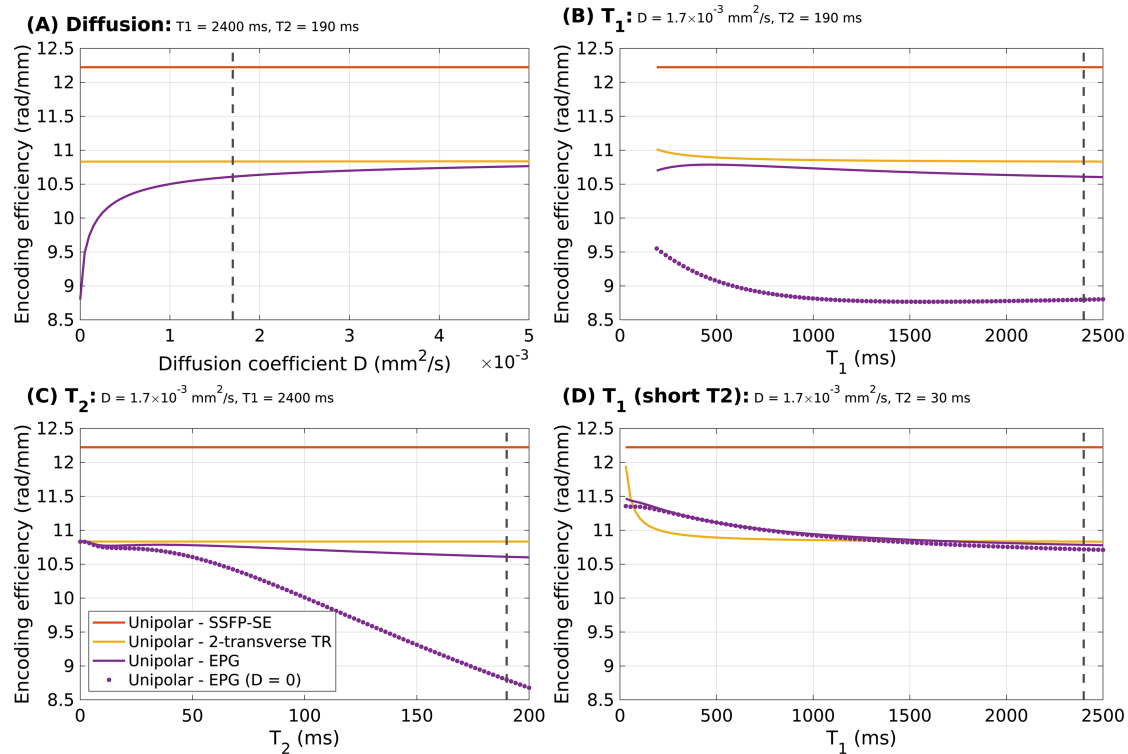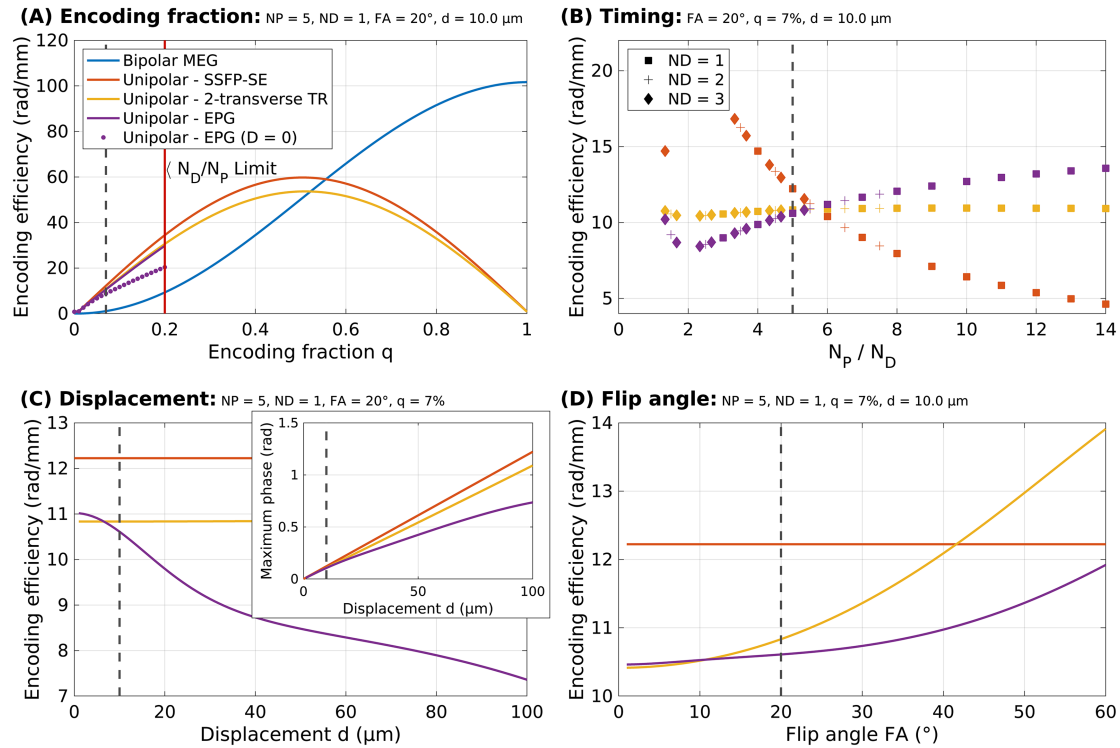
FIGURE 5 Encoding efficiency comparison of unipolar MRE in the simplified phase-contrast approximation (red), the two-transverse TR approximation (yellow), and the full EPG simulation (violet). The dashed line denotes the default parameter assumed in all simulations, ie, $f = 35$ Hz, NP = 5, ND = 1 (TR = 5.71 ms), q = 7% and G = 20 mT/m, if not otherwise stated. Dependencies are plotted as a function of (A) diffusion coefficient, (B) T_1 relaxation for long T_2 (190 ms), (C) T_2 relaxation for long T_1 (2400 ms) and (D) T_1 relaxation for short T_2 (30 ms). In (A), the approach of the full EPG simulation towards the two-transverse TR approximation for strong diffusion can be appreciated. For (B)-(D), full EPG simulations for unipolar MRE neglecting diffusion (dotted violet) are shown to demonstrate deviation of the encoding efficiency due to interference of high order, motion-sensitive configuration states. Compared with full EPG simulations, the two-transverse TR approximation can account for more than 90% of the encoding efficiency in the presence of diffusion

constructively. For increasing ratios, the SSFP-SE contribution shows declining encoding efficiency. The two-transverse TR approximation predicts approximately constant behavior, whereas the full EPG simulation shows increasing encoding efficiency with increasing N_P/N_D ratio above two. The behavior of the encoding efficiency is reversed if N_P/N_D ratios below five are considered. Figure 6C investigates the dependency of the magnitude of the complex encoding efficiency as a function of wave displacement. Both the spin echo and the two-transverse TR approximation show constant encoding efficiency, thus displacements are encoded linearly in the signal phase. The full EPG simulation shows nonlinear behavior, especially for displacements above 15 μm. The inset depicts the maximal signal phase $|\epsilon d|$ for the same range of displacements from 0 to 100 μm, again showing the linearity of encoding in the SSFP-SE and two-transverse TR approximation. The full EPG solution is nonlinear but monotonously increasing with displacement. Finally, the dependency of the encoding efficiency of unipolar MRE as a function of the flip angle is investigated in Figure 6D. With increasing flip angle, both full EPG and the two-transverse TR approximation show an increase in encoding efficiency, while the SSFP-SE contribution remains constant. The dependency of the encoding efficiency phase angle on the imaging parameters is shown in Figure S4.

4.2 | Phantom results

In Figure 7, the results of the quantitative parameter mapping for (A) T_1 and T_2, and (B) ADC and FA are displayed. T_1 is found to be approximately constant over the whole phantom (2425 ± 33 ms), while T_2 differs significantly between background (193 ± 25 ms) and inclusions (632 ± 33 ms). The ADC is found to be approximately constant over the whole phantom ([1.68 ± 0.31] x 10^{-3} mm^2/s). FA is close to zero, consistent with the assumption of isotropic diffusion. ROI average and standard deviation for the inclusions, background and the whole phantom are given in Table S2. In Figure 7C, the magnitude and phase of the local encoding efficiency are shown based on the determined T_1 and T_2 map; however, diffusion effects are neglected. Substantial encoding efficiency differences between background ($|\epsilon|$ = 8.77 ± 0.30 rad/mm, $\angle\epsilon$ = 0.192 ± 0.008 rad) and inclusions ($|\epsilon|$ = 5.76 ± 0.13 rad/mm, $\angle\epsilon$ = 0.276 ± 0.009 rad) of ~52% can be observed. Figure 7D shows the encoding efficiency taking a constant diffusion coefficient of 1.7 x 10^{-3} mm^2/s into account. Here, the encoding efficiency of the background

FIGURE 6 Encoding efficiency comparison of unipolar MRE in the simplified phase-contrast approximation (red), the two-transverse TR approximation (yellow) and the full EPG simulation (violet). The dashed line denotes the default parameter assumed in all simulations, ie, $T_1 = 2.4$ s, $T_2 = 190$ ms, $D = 1.7 \times 10^{-3}$ mm^2/s, $f = 35$ Hz and $G = 20$ mT/m. dependencies are plotted for (A) encoding fraction, (B) number phase offsets and delay, (C) displacement and (D) flip angle. In (a), conventional MRE with bipolar MEGs is shown in blue as well as the full EPG simulation neglecting diffusion (dotted violet). Unipolar MRE shows a linear dependency on the encoding efficiency as displacements are directly encoded, whereas bipolar MEGs encode the velocity and respectively scale proportional to q^2. The refocusing of higher order configuration states leads to pronounced interference, which results in the dependency on (B) sequence timing as well as nonlinear displacement encoding (C). The inset in (C) shows the magnitude of the product of displacement and encoding efficiency. Deviations from the two-transverse TR approximation are minor in the small displacement domain (<20 µm) showing that encoding is dominated by refocused 1st order contributions

($|\varepsilon| = 10.605 \pm 0.024$ rad/mm, $\angle\varepsilon = 0.006 \pm 0.013$ rad) and inclusions ($|\varepsilon| = 10.412 \pm 0.007$ rad/mm, $\angle\varepsilon = -0.095 \pm 0.005$ rad) deviates by less than 2%, allowing treatment of the encoding efficiency as homogenous over the phantom. ROI average and standard deviation of magnitude and phase of the encoding efficiency, including diffusion effects for the inclusions, background and the whole phantom, are given in Table S2.

In Figure 8, (A) signal magnitude and (B) the real-part of the complex displacement field for one representative slice and through-plane direction are shown for both unipolar and conventional MRE at 35 and 70 Hz actuation frequency. The top row corresponds to the magnitude images obtained from a single phase-offset, slice and encoding direction without averaging. Pronounced intra-voxel phase dispersion-based signal drop can be observed in the unipolar MRE scan due to the high encoding efficiency compared with conventional GRE-MRE. In addition, a reduction in signal magnitude can be observed at the boundaries of the phantom due to transmit field inhomogeneity and the strong flip angle dependency of the time-reversed SSFP sequence. The central row corresponds to single scans, whereas the bottom row denotes averaged displacement fields for increased SNR. Both conventional and unipolar MRE show qualitatively equivalent wave patterns. The SNR of the conventional MS MRE scan is considerably lower than unipolar MRE, as can be directly appreciated from the graininess of the displacement field of the single scan, which is strongly reduced in the case of 20-fold averaging. The averaged magnitude of the ratio of unipolar to conventional displacement fields is 94.4% at 35 Hz, showing good quantitative agreement. At 70 Hz actuation, displacement fields reconstructed from unipolar MRE are slightly lower, with an average ratio of 84.0%.

In Figure 9, the magnitude of the complex shear stiffness obtained through a FEM-based inversion algorithm is shown at 35 and 70 Hz actuation frequency for conventional and unipolar MRE in the case of single and averaged scans. Generally, background as well as the soft inclusions (left inclusions) are well recovered, independent of the technique and the number of averages acquired. Conventional MRE, however, fails to obtain reasonable stiffness values at 35 Hz for the two stiffest inclusions (right inclusions), while unipolar MRE already predicts their high stiffness with only a single scan. In the 20-fold averaged conventional MRE scan, the increased stiffness of the two right inclusions is well observed. At 70 Hz, both techniques are in good agreement, with only slight underestimation of the shear stiffness of the stiffest inclusion (bottom right) in the case of the single average, conventional MRE scan.
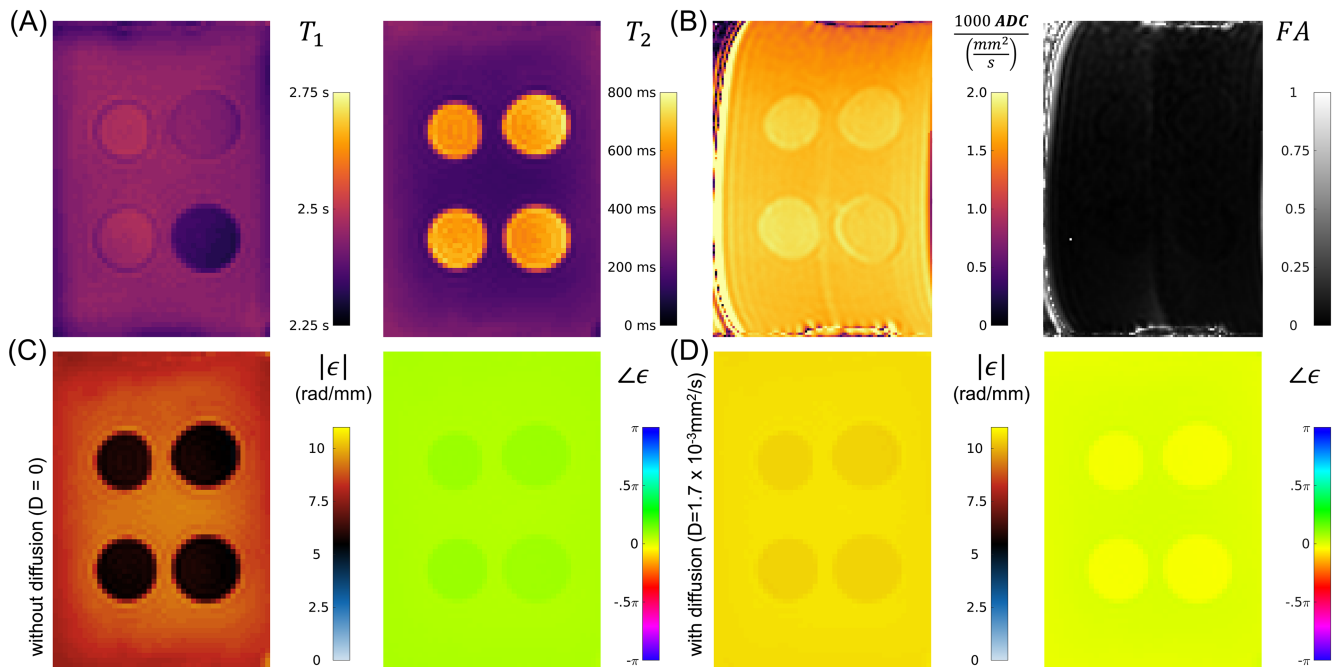
FIGURE 7 Quantitative parameter maps for (A) T_1 and T_2, (B) ADC and FA. T_1 and ADC are approximately constant over the phantom and are 2425 ± 33 ms and (1.68 ± 0.31) x 10^{-3} mm²/s, respectively. FA is 0.042 ± 0.022 over the whole phantom, which is consistent with the assumption of isotropic diffusion. T_2 of inclusions is elevated (632 ± 33 ms) compared with the background (193 ± 25 ms). In (C), magnitude and phase of the encoding efficiency is shown as a map neglecting diffusion but taking T_1/T_2 from (A) into account. In (D), the encoding efficiency incorporating constant diffusion (1.7 x 10^{-3} mm²/s) is shown. Compared with (C), differences in encoding efficiency including diffusion effects are below 2%

In Figure 10, the ROI-averaged magnitudes of the complex shear stiffness are displayed, against the OSS-SNR determined over the same ROI. Conventional MRE is denoted by open circles, while unipolar MRE is shown as squares. Values for single and averaged scans are given in Table S3. For 35 Hz, the OSS-SNR of unipolar MRE without averaging is higher than the OSS-SNR of the 20-fold averaged conventional scan for all regions. At 70 Hz, the single average unipolar MRE acquisition is comparable with an 8- to 10-fold averaged conventional MRE scan. Stiffness of inclusions 1 and 2 as well as the background are well recovered independent of the number of averages and technique. Conventional MRE qualitatively fails to predict the stiffness of inclusions 3 and 4, showing higher stiffness for the softer, third inclusion. Through averaging, the stiffness of inclusions 3 and 4 determined by conventional MRE increases significantly by 54% (inclusion 3) and 179% (inclusion 4) at 35 Hz and by 3.8% and 10.3% at 70 Hz, respectively. In conventional MRE and at 35 Hz, the stiffness of inclusion 3 reaches a plateau after 11 averages, while the stiffness of inclusion 4 increases even after 20 averages. With unipolar MRE, the change in stiffness is below 0.3% for the first three inclusions as well as the background. Change in stiffness for inclusion 4 is 6.2% at 35 Hz and 1.9% at 70 Hz, and reaches a plateau after five averages in both cases.

5 | DISCUSSION

In this work, we have proposed a novel MR elastography sequence based on time-reversed spoiled SSFP, which utilizes the spoiling gradients as highly efficient unipolar MEGs. We have motivated the fundamental encoding principle of unipolar MRE through analogies to phase-contrast MRI and have described an extension of the two-transverse TR approximation developed for DW-SSFP to account for lowest order spin-history effects.

The theoretical predictions of the proposed approximations have been compared with full EPG simulations in a comprehensive parameter study. It was found that longer T_1 and T_2 values as well as lower diffusion generally leads to a reduction in encoding efficiency. We attribute this finding to the destructive interference of an increasing number of refocused echo pathways. Contrary to conventional MRE, unipolar MRE encodes displacements d nonlinearly into the signal phase, as echo pathways with different motion sensitivities are mixed. However, we have identified a linear encoding domain, which is approximately given by $\Delta k |d| \lesssim 10\%$. Since the contributions of the different echo pathways are dependent on relaxation and sequence parameters, it is safe to assume that the displacement range that is mapped linearly to the signal phase will be dependent on these parameters as well. This can also be appreciated in Figure S2, which is the short T_1/T_2 equivalent of Figure 6 (T_1 = 300 ms, T_2 = 30 ms). There, the linear encoding domain is approximately twice as large and given by $\Delta k |d| \lesssim 20\%$. Since encoding efficiency was found to be monotonically decreasing, unipolar MRE shows heightened sensitivity to low displacement amplitudes.
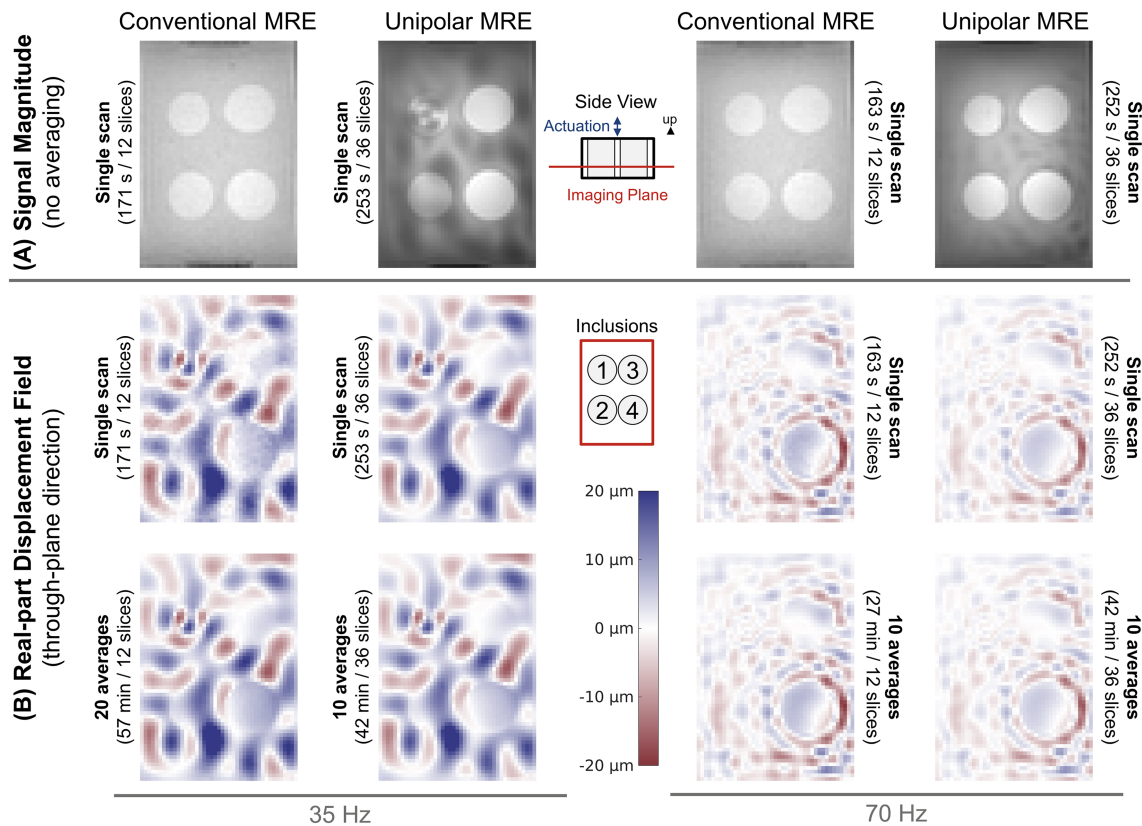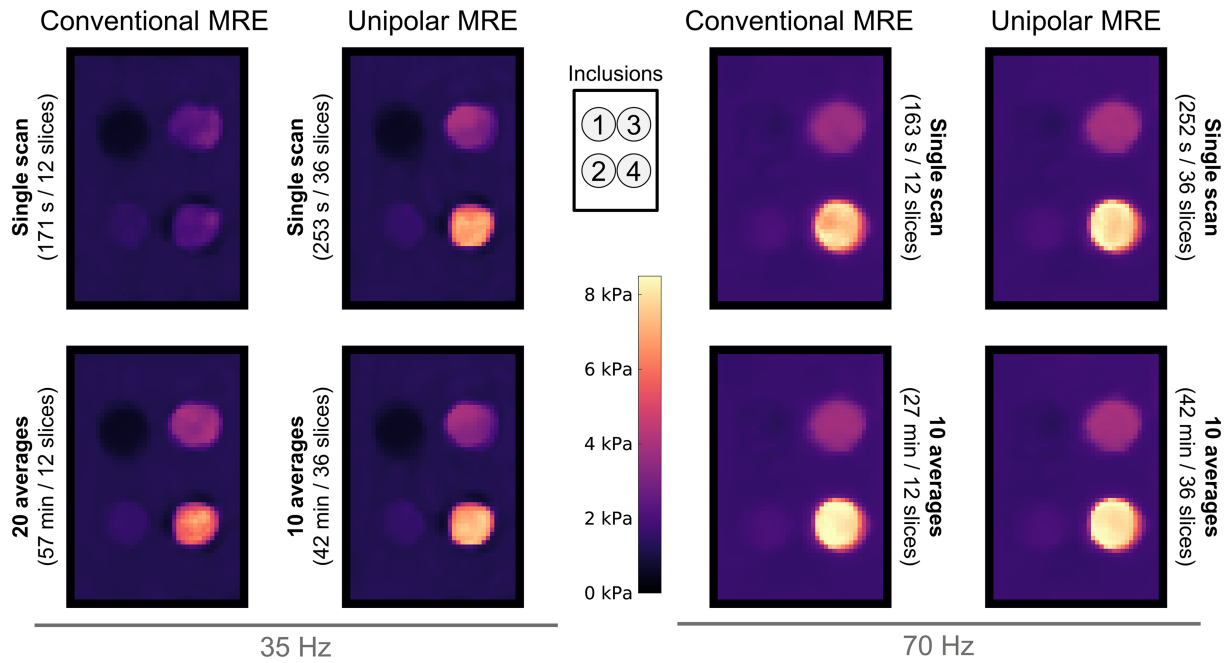
FIGURE 8 (A) Comparison of the magnitude images of conventional GRE- and unipolar MRE at 35 and 70 Hz frequency for one phase-offset, encoding direction and slice. Compared with conventional GRE-MRE, pronounced intra-voxel phase-dispersion and B_1^+-dependent contrast is visible. (B) Comparison of the real part of the complex shear displacement field in through-plane direction with and without averaging. The displacement fields are qualitatively and quantitatively in good agreement. At 70 Hz, unipolar MRE shows slightly reduced wave displacements throughout the phantom compared with conventional MRE. Conventional MRE shows considerable displacement noise in the single scan compared with both unipolar MRE and averaged conventional MRE, respectively. The top center sketch depicts the phantom from a side view including the alignment of the imaging plane as well as the actuator placement

In the case of conventional GRE-MRE, the encoding efficiency decreases as the duration of the encoding gradient is reduced, even if a finite moment for each of the two lobes is assumed. By contrast, unipolar MRE shows a finite encoding efficiency in the case of the infinitesimal model given by Equation 12. This demonstrates the uniqueness of unipolar MRE, which, unlike conventional GRE-MRE, splits encoding over two (and more) TR periods, thus effectively storing spin positions in the phase of the MR signal during the first TR and subtracting the updated position with the second TR. Analogous to SE sequences with single gradient lobes[47] or displacement encoding with stimulated echoes (DENSE),[55] it is precisely the mixing time between the two encoding steps that leads to the high motion sensitivity of the unipolar MRE sequence, and time-reversed SSFP sequences in general. This relationship also manifests itself in the comparison of encoding efficiencies as a function of encoding fractions q in Figure 6A, where unipolar MRE shows a linear increase in encoding efficiency as a function of the MEG duration, whereas conventional bipolar MEGs follow a quadratic behavior in the small q domain.

Note that the quadratic behavior is reminiscent of the encoding of displacement velocities, while the linear relationship arises from the direct encoding of displacement.[3] Since the gradient strength G is kept constant in the plot, the moment Δk vanishes for unipolar MRE with q → 0 and thus also its encoding efficiency.

A direct consequence of encoding displacements in unipolar MRE (as opposed to encoding displacement velocities with conventional MRE) is the dependency of the encoding efficiency on sequence timing rather than encoding fraction (assuming Δk is kept constant). The SSFP-SE contribution to unipolar MRE is shown to decrease with increasing N_P/N_D ratio, as displacements between successive encoding/decoding steps become more and more similar. The full EPG simulations, on the other hand, show increasing encoding efficiency with increasing N_P/N_D ratio. We speculate that the interference of echo pathways is reduced as successive TR periods accumulate more and more similar motion phases. The parameter study also revealed an increase in encoding efficiency with increasing flip angle. Since an increase in flip angle leads to a reduction of the population of high-spatial frequency states, this finding is in general accordance with the dependency on T_1, T_2 and diffusion. Furthermore, it supports the hypothesis of destructive interference of motion encoding due to differences in motion sensitivity of echo pathways. Contrary to bSSFP-based MRE,[6,21,22] the encoding efficiency of unipolar MRE is independent of off-resonance, as dephasing and refocusing configuration states experience opposite phase accrual. Thus, each echo pathway shows the same dependency on off-resonance $\Delta\omega$, which is given by

FIGURE 9 Comparison of the magnitude of the shear stiffness for conventional GRE-MRE and the proposed unipolar MRE scheme for 35 and 70 Hz actuation frequency with and without averaging. The reported maps are average stiffness values over the six innermost slices. While conventional MRE fails to predict the stiffness of the stiffest inclusions (right inclusions) in the single scan, the increased SNR in unipolar MRE allows recovery of these inclusions without additional averaging
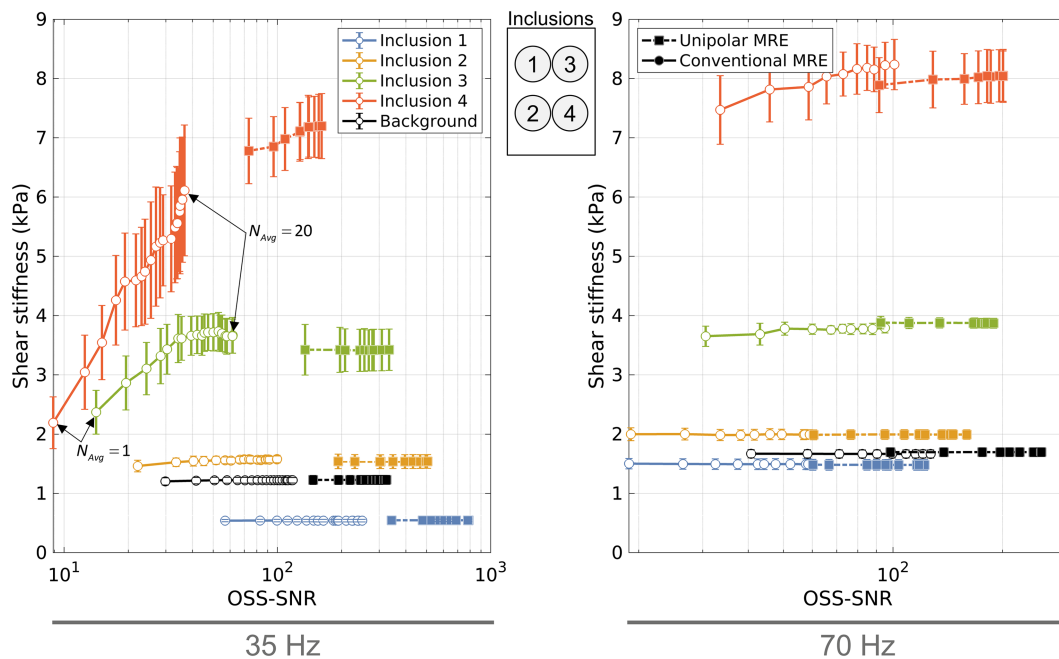
FIGURE 10 Comparison of the region of interest (ROI)-averaged shear stiffness (bars denote the standard deviation over the ROI) obtained with conventional GRE-MRE (solid line, circles) and the proposed unipolar MRE (dashed line, squares) at 35 and 70 Hz actuation frequency. The x-axis denotes the average octahedral shear strain-SNR (OSS-SNR) for each ROI. Sample averaging was performed to increase the SNR in both unipolar and conventional MRE to demonstrate the influence of SNR on the reconstructed shear stiffness. Here, the left-most data-points in each series correspond to the single-scan case, where each successive point increases the number of sample averages up to $N_{Avg} = 20$. While the stiffness of soft inclusions (numbers 1 and 2) and the background are found to be independent of the OSS-SNR, stiff inclusions (numbers 3 and 4) depend on the number of sample averages for conventional MRE at 35 Hz. Due to the increased OSS-SNR of unipolar MRE, even without averaging, unipolar MRE can directly capture the stiffness of these inclusions

$\exp\{i\Delta\omega(T_E - T_R)\}$. Thus, in equivalence to conventional spoiled GRE-MRE, off-resonance leads to an image phase offset, which is independent of the wave-phase offset and is removed once the Fourier transformation over wave phases is performed.

Since unipolar MRE uses the spoiling gradients as MEGs, the sequence TR can be considerably reduced compared with conventional GRE-MRE. Given that time-reversed spoiled SSFP sequences cannot be used with interleaved MS acquisitions, the sequence TR is generally much shorter than typical T_2 values. A Taylor series expansion of the echo signal in $\exp\{-T_R/T_2\}$ is at first sight not feasible. Nonetheless, the two-transverse TR approximation proves to be valuable in describing the encoding efficiency of the unipolar MRE acquisition, especially within the linear encoding regime. This can be appreciated from the closeness of predicted encoding efficiency of the two-transverse TR approximation and the full EPG simulations in Figures 5 and 6, as well as the close coincidence of the displacement fields in the phantom experiments depicted in Figure 8. While differences between the full EPG and the two-transverse TR approximation certainly persist in theory, we believe that the attenuation of configuration states is not only due to diffusion and transverse relaxation but is complemented by intra-voxel phase dispersion (see below) additionally driving the sequence closer to the two-transverse TR solution.

The propagator definition in Equation 16 assumes periodic bulk motion. From conventional MRE it is known that the variation of the displacement field within one voxel leads to intra-voxel phase dispersion (IVPD) and thus signal attenuation.[56,57] In the 1D case of a propagating plane-wave with wavelength λ, signal attenuation by IVPD in the conventional MRE case can be estimated to be

$$S \approx S_0 \left| \operatorname{sinc}\left(\pi \frac{\Delta x}{\lambda} \epsilon r_0\right) \right|, \tag{31}$$

where S_0 denotes the expected signal without IVPD and S the attenuated signal.[8,57] In the case of unipolar MRE, intra-voxel variations of the displacement field can be treated using the spatially resolved EPG, which assumes each spatial position as independent EPG simulations.[58] The echo signal can then be approximately expressed as the average of sub-voxel signals, each being a superposition of refocused echo pathways. Since summation over echo pathways and spatial averaging can be exchanged, IVPD in unipolar MRE can not only be discussed as a total effect of signal attenuation, it can also be studied for each echo pathway separately. As the motion sensitivity of configuration states increases proportionally to their spatial frequency, each echo pathway accumulates a different motion-dependent phase. From Equation 31 it becomes clear that echo pathways involving higher order configuration states will exhibit stronger attenuation due to their increased phase dispersion. Thus, similar to diffusion, the presence of IVPD is expected to reduce the contributions of higher order configuration states to the steady-state signal and therefore reduces the influence of tissue, experiment and sequence properties on the encoding efficiency.

In the derivation and analysis of unipolar MRE, the assumption of isotropic diffusion was made. While the DTI measurements support this assumption in the phantom used, a discussion of anisotropic diffusion is necessary when unipolar MRE is employed in vivo. McNab and Miller extended the two-transverse TR approximation for anisotropic DW-SSFP by replacing the exponent of the diffusion propagator by its respective anisotropic form.[44] Weigel et al later introduced anisotropic diffusion in the context of the EPG formalism.[59] Both approaches can be equally used here. Since the encoding direction and thus diffusion sensitization is held constant in successive TRs, the diffusion coefficient D that enters into the 1D diffusion propagator (Equation 20) can be simply replaced by the projection of the diffusion tensor $\hat{D}$ on the encoding direction $\vec{e}$

$$D = \vec{e}^{\mathsf{T}} \hat{D} \vec{e}. \tag{32}$$

Thus, in the presence of anisotropic diffusion, encoding direction-dependent attenuation of configuration states, and with these direction-dependent encoding efficiencies, are expected to occur.

In the nonlinear regime (here $\Delta k|d| > 10\%$), full EPG simulations show a monotonous decline in encoding efficiency, which leads to systematic underestimation of large displacements (Figure 6C). Since the dependency on the displacement amplitude is found to be monotonous within the relevant displacement domain, a bidirectional relationship is likely to exist. With exact knowledge of the B_1^+ field as well as tissue parameters within the ROI, full EPG simulations with different displacement amplitudes can be performed to correct the displacement fields, eg, via a look-up-table approach. This also holds for the variation in phase angle (as observed in Figure S4).

The sequence has been validated in a phantom study against a conventional GRE-MRE sequence at two driving frequencies, where displacement fields were found to be in excellent agreement. We attribute the remaining differences to differences in the slice profile of MS and 3D acquisitions as well as to residual differences in encoding efficiency due to local relaxation parameter variations. Especially at low driving frequency, the displacement noise is visually higher in the conventional MRE scan than in unipolar MRE, which is also confirmed by the OSS-SNR calculations. The low SNR of the conventional MRE scan leads to underestimation of the stiffness of the two stiffest inclusions. Here, conventional MRE without averaging even fails to qualitatively predict the elevated stiffness of inclusion 4 compared with inclusion 3 (Figure 9). The stiffness of inclusions 1 and 2 as well as the phantom background were found to be in excellent agreement between unipolar and conventional MRE.

Through averaging, the SNR of the conventional MRE scan could be successfully increased to the point of close agreement of recovered stiffness values with unipolar MRE. At 35 Hz, however, even 20-fold averaging of the conventional MRE scan did not provide sufficient SNR to allow estimation of the stiffness of the two stiffest inclusions. Minor differences in the order of 0.2 kPa persist, however, for inclusion 3 at 35 Hz, and

also the two stiffest inclusions at 70 Hz. We believe these differences to be again attributable to slice profile differences, since the high stiffness of the inclusions leads to very low spatial derivatives and thus renders the inversion especially sensitive to geometrical mismatches.

In this study, conventional MRE was performed with fewer slices compared with unipolar MRE (12 vs. 36 slices) to keep scan durations within acceptable ranges. Since unipolar MRE uses slab excitation of the whole phantom and phase encoding in the slice-encoding direction, SNR of 3D unipolar MRE is $\sqrt{N_S}$-fold higher than a respective 2D scan with equal TR, where N_S denotes the number of phase-encoding steps in the slice direction. Accordingly, the SNR of the unipolar MRE scan was $\sqrt{3}$ higher, equaling 3-fold averaging. An OSS-SNR efficiency adjusted for the slice acquisition technique can be defined, which relates the OSS-SNR to the total acquisition duration T_{Tot} and accounts for the number of averages N_{Avg} and slices N_S. For conventional MRE, where MS acquisition is performed, the OSS-SNR efficiency can be defined as

$$oss\text{-}snr_{MS} = \frac{OSS\text{-}SNR\sqrt{N_{Avg}}N_S}{T_{Tot}}. \tag{33}$$

The use of slab excitation (3D) in unipolar MRE leads to

$$oss\text{-}snr_{3D} = \frac{OSS\text{-}SNR\sqrt{N_{Avg}N_S}}{T_{Tot}}. \tag{34}$$

At 35 Hz, this results in an OSS-SNR efficiency of 120 min^{-1} for conventional MRE and 226 min^{-1} for unipolar MRE for a single slice and average (at 70 161 min^{-1} and 1355 min^{-1}, respectively). The OSS-SNR was determined over the whole phantom for a single scan. Hence, for the acquisition of a single slice and average, unipolar MRE is approximately twice as effective at 35 Hz than conventional GRE-MRE, and more than 8-fold at 70 Hz.

Reconstructed stiffness in unipolar MRE converges after 5-fold averaging compared with at least 20-fold averaging with conventional MRE. This corresponds to a per-slice speed-up of at least 8-fold in the case of 35 Hz, and 4-fold in the case of 70 Hz, when taking the acquisition speed-up of factor 2 per slice into account. Based on the OSS-SNR, single-average unipolar MRE corresponds to more than 40-fold acceleration, as it shows considerably higher OSS-SNR at 35 Hz than the 20-fold averaged conventional MRE scan. At 70 Hz, unipolar MRE would be up to 18-fold faster when compared with conventional MRE.

In the phantom study, the actuation strength was specifically chosen to remain within the linear encoding regime. While in conventional MRE the encoding efficiency can be reduced by gradient scaling or lowering the encoding fraction,[6] in unipolar MRE spoiling and motion sensitivity are coupled. Thus, a reduction of encoding efficiency to remain within the linear encoding regime is not feasible. Changes to the duration of the encoding gradient at constant zeroth moment only leads to minor reductions in encoding efficiency. Thus, if linear encoding is intended, displacement amplitudes must be chosen accordingly.

The motion propagator in Equation 18 cannot only be used for the simulation of unipolar MRE, but for sequences with periodic motion in general. Since the propagator describes motion sensitivity of configuration states subject to a generalized trapezoidal gradient, concatenation of the propagator allows performing EPG simulations with bipolar or flow-compensated gradients. Hence, it can be employed to study spin-history effects in conventional 3D GRE-MRE with short TRs or the influence of RF spoiling and its efficiency in canceling higher order echo pathways.

Previous work by Scheffler et al has described an encoding concept similar to unipolar MRE to induce an "oscillating steady-state" in a spoiled SSFP sequence with readout of the F_{-2}, F_{-1}, F_0 and F_1 configuration states.[60] Contrary to our objective to encode and extract the full 3D shear displacement field, Scheffler et al's concept aimed at studying the effect of alternating RF-phases on the signal amplitude of SSFP-based sequences. While unipolar MRE can be seen to directly build on their encoding concept, it differs from the work by Scheffler et al in the following important aspects: (i) unipolar MRE is designed to readout the F_{-1} state only in order to reduce the TR and accelerate MRE acquisition to the fullest extent possible. A dual-echo approach as employed in Scheffler et al's work for aforementioned purposes could possibly be employed to (a) reduce relaxation time dependencies with combined displacement estimation using the high motion sensitivity of the F_{-1} state and the relaxation parameter insensitive F_0 state, and (b) to combine the technique with double-echo-steady-state (DESS) relaxometry.[26] (ii) The work by Scheffler et al is based on the description of a steady-state that oscillates between two TRs. Our steady-state is composed of N_P distinct signals, which is closer to the description of pseudo-steady states by Assländer et al and Amthor et al.[61,62] (iii) Spoiling and readout gradients are uncoupled to allow for the sensitization of the sequence to the different motion components of the shear wave field. (iv) Our formulation of steady states is based on the EPG formalism. The two-transverse TR approximation describes the signal to the second order in $\exp\{-T_R/T_2\}$ and thus makes assumptions on the contributing echo pathways. On the other hand, Scheffler et al developed a signal model for small perturbations of the accumulated phase during a TR period without making assumptions on relaxation properties. Transferring their approach to unipolar MRE, it becomes a model to describe motion encoding for small displacements in the case of $N_P = 2$. An extension of their work to more than two states is beyond the scope of this work; however, it would provide a valuable addition to the understanding of encoding in unipolar MRE in the absence of diffusion or IVPD.

In the present work, Hadamard encoding has been used to allow for the extraction of the 3D volumetric displacement field. It should be noted that unipolar MRE is not restricted to Hadamard encoding alone—all encoding schemes lacking a separate reference scan without motion

sensitization can be used. Clinically, MR elastography is often performed on a small set of discontinuous 2D slices with only through-plane motion sensitization.[63,64] In unipolar MRE, slab excitation and phase encoding in the slice direction can be replaced by single slice excitation. Interleaved MS acquisitions cannot be paired with unipolar MRE as it is described here, as spoiling gradients in consecutive TR periods will accumulate and change the overall spoiling area as well as the motion sensitization scheme.

While the present work has focused on the theoretical foundations and phantom validation of unipolar MRE, future work is required to assess the utility of the method in vivo. The high intended motion sensitivity of unipolar MRE requires careful consideration and provisions depending on the target anatomy, in particular if physiological and patient motion is present. Accordingly, unipolar MRE is expected to require breath-holding in the case of thoracic and abdominal applications. To address cardiac-related motion, artifact reduction techniques such as averaging or gating may need to be incorporated.[65] In brain and spine, the pulsatile CSF flow is expected to be encoded by unipolar MRE, potentially interfering with displacement encoding.[36,42,66] However, since SNR is much higher in unipolar MRE than in a comparable conventional GRE-MRE sequence, a combination of compressed sensing and self-gating techniques is envisaged.[13,65,67,68] Overall, the influence of physiological and patient motion on the steady-state signal and resulting changes in encoding efficiency remains to be understood. In addition, in vivo parametric mapping of T_1, T_2 and ADC would be required for the tissue of interest to estimate their impact on the local encoding efficiency. While the phantom results and theoretical considerations suggest that relaxation effects are not critical, these results need to be confirmed in vivo.

Given the considerations above, a first application of unipolar MRE could focus on brain, where mechanical attenuation by the skull results in low displacement amplitudes necessitating high encoding efficiency and SNR.

In the future, unipolar MRE might prove valuable for multi-frequency MRE, when different actuation frequencies are acquired consecutively. This is especially the case for low driver frequencies as the SNR is significantly increased with unipolar MRE compared with conventional MRE with fractional encoding. At high frequencies, however, unipolar MRE loses its advantage over conventional MRE as encoding fractions typically become much larger and acceleration is limited by the combined duration of RF pulse and readout, not by the MEG duration.

6 | CONCLUSION

We have proposed a novel MR elastography sequence termed "unipolar MRE", which utilizes the spoiling gradients of a time-reversed SSFP sequence to acquire the full 3D shear displacement field. Compared with conventional GRE-MRE, unipolar MRE offers significantly reduced TRs with comparable or even increased displacement encoding efficiency. Accordingly, 4- to 8-fold faster acquisitions at equal or higher OSS-SNR can be achieved.

ORCID

Christian Guenthner https://orcid.org/0000-0001-8707-7016
Marian Troelstra https://orcid.org/0000-0001-6748-4810
Robbert J.H. van Gorkum https://orcid.org/0000-0003-1072-0477
Mareike Gastl https://orcid.org/0000-0002-7854-8418
Ralph Sinkus https://orcid.org/0000-0002-6093-1654
Sebastian Kozerke https://orcid.org/0000-0003-3725-8884

REFERENCES

1. Muthupillai R, Lomas D, Rossman P, Greenleaf J, Manduca A, Ehman R. Magnetic resonance elastography by direct visualization of propagating acoustic strain waves. *Science*. 1995;269(5232):1854-1857.

2. Moran PR. A flow velocity zeugmatographic interlace for NMR imaging in humans. *Magn Reson Imaging*. 1982;1(4):197-203.

3. Guenthner C, Kozerke S. Encoding and readout strategies in magnetic resonance elastography. *NMR Biomed*. 2018;31(10):e3919.

4. Sinkus R, Lorenzen J, Schrader D, Lorenzen M, Dargatz M, Holz D. High-resolution tensor MR elastography for breast tumour detection. *Phys Med Biol*. 2000;45(6):1649-1664.

5. Le Bihan D, Poupon C, Amadon A, Lethimonnier F. Artifacts and pitfalls in diffusion MRI. *J Magn Reson Imaging*. 2006;24(3):478-488.

6. Rump J, Klatt D, Braun J, Warmuth C, Sack I. Fractional encoding of harmonic motions in MR elastography. *Magn Reson Med*. 2007;57(2):388-395.

7. Garteiser P, Sahebjavaher RS, Ter Beek LC, et al. Rapid acquisition of multifrequency, multislice and multidirectional MR elastography data with a fractionally encoded gradient echo sequence. *NMR Biomed*. 2013;26(10):1326-1335.

8. Guenthner C, Runge JH, Sinkus R, Kozerke S. Analysis and improvement of motion encoding in magnetic resonance elastography. *NMR Biomed*. 2018;31(5):e3908.

9. Ernst RR, Anderson WA. Application of Fourier transform spectroscopy to magnetic resonance. *Rev Sci Instrum*. 1966;37(1):93-102.

10. Zur Y, Wood ML, Neuringer LJ. Spoiling of transverse magnetization in steady-state sequences. *Magn Reson Med*. 1991;21(2):251-263.

11. Runge J, Hoelzl S, Sudakova J, et al. A Novel MR Elastography transducer concept based on a rotational eccentric mass: the gravitational transducer. *Proc Intl Soc Mag Reson Med*. 2017;25:1369.

12. Guenthner C, Sethi S, Dokumaci AS, Sinkus R, Kozerke S. Ristretto MRE: a generalized multi-shot GRE-MRE sequence. *Proc Intl Soc Mag Reson Med*. 2018;26:5584.

13. Guenthner C, Kozerke S. MEG-navigators for motion detection and quality assurance in MR elastography. *Proc Intl Soc Mag Reson Med*. 2018;26:221.

14. Klatt D, Yasar TK, Royston TJ, Magin RL. Sample interval modulation for the simultaneous acquisition of displacement vector data in magnetic resonance elastography: theory and application. *Phys Med Biol*. 2013;58(24):8663-8675.

15. Klatt D, Johnson CL, Magin RL. Simultaneous, multidirectional acquisition of displacement fields in magnetic resonance elastography of the in vivo human brain. *J Magn Reson Imaging*. 2015;42(2):297-304.

16. Nir G, Sahebjavaher RS, Sinkus R, Salcudean SE. A framework for optimization-based design of motion encoding in magnetic resonance elastography. *Magn Reson Med*. 2015;73(4):1514-1525.

17. Yasar TK, Klatt D, Magin RL, Royston TJ. Selective spectral displacement projection for multifrequency MRE. *Phys Med Biol*. 2013;58(16):5771-5781.

18. Johnson CL, McGarry MDJ, Van Houten EEW, et al. Magnetic resonance elastography of the brain using multishot spiral readouts with self-navigated motion correction. *Magn Reson Med*. 2013;70(2):404-412.

19. Johnson CL, Holtrop JL, McGarry MDJ, et al. 3D multislab, multishot acquisition for fast, whole-brain MR elastography with high signal-to-noise efficiency. *Magn Reson Med*. 2014;71(2):477-485.

20. Guenthner C, Runge JH, Sinkus R, Kozerke S. Simultaneous multislice acquisition for magnetic resonance elastography. *Proc Intl Soc Mag Reson Med*. 2017;25:1132.

21. Rump J, Warmuth C, Braun J, Sack I. Phase preparation in steady-state free precession MR elastography. *Magn Reson Imaging*. 2008;26(2):228-235.

22. Bieri O, Maderwald S, Ladd ME, Scheffler K. Balanced alternating steady-state elastography. *Magn Reson Med*. 2006;55(2):233-241.

23. Klatt D, Asbach P, Rump J, et al. In vivo determination of hepatic stiffness using steady-state free precession magnetic resonance elastography. *Invest Radiol*. 2006;41(12):841-848.

24. Heule R, Ganter C, Bieri O. Triple echo steady-state (TESS) relaxometry. *Magn Reson Med*. 2014;71(1):230-237.

25. Heule R, Celicanin Z, Kozerke S, Bieri O. Simultaneous multislice triple-echo steady-state (SMS-TESS) T1, T2, PD, and off-resonance mapping in the human brain. *Magn Reson Med*. 2018;80(3):1-13.

26. Welsch GH, Scheffler K, Mamisch TC, et al. Rapid estimation of cartilage T2 based on double echo at steady state (DESS) with 3 Tesla. *Magn Reson Med*. 2009;62(2):544-549.

27. McNab JA, Miller KL. Steady-state diffusion-weighted imaging: theory, acquisition and analysis. *NMR Biomed*. 2010;23(7):781-793.

28. Weigel M. Extended phase graphs: dephasing, RF pulses, and echoes - pure and simple. *J Magn Reson Imaging*. 2015;41(2):266-295.

29. Guenthner C, Sethi S, Dokumaci AS, Sinkus R, Kozerke S. Ultra-fast 4D MR elastography using down-stream echoes. *Proc Intl Soc Mag Reson Med*. 2018;26:1073.

30. Bernstein MA, King KF, Zhou XJ. *Handbook of MRI Pulse Sequences*. Amsterdam: Elsevier Academic Press; 2004.

31. Buxton RB. The diffusion sensitivity of fast steady-state free precession imaging. *Magn Reson Med*. 1993;29(2):235-243.

32. Scheffler K. A pictorial description of steady-states in rapid magnetic resonance imaging. *Concepts Magn Reson*. 1999;11(5):291-304.

33. Guenthner C, Sethi S, Troelstra M, Dokumaci AS, Sinkus R, Kozerke S. Ristretto MRE: a generalized multi-shot GRE-MRE sequence. *NMR Biomed*. 2019;32(5):e4049.

34. Gyngell ML. The application of steady-state free precession in rapid 2DFT NMR imaging: FAST and CE-FAST sequences. *Magn Reson Imaging*. 1988;6(4):415-419.

35. Elster AD. Gradient-echo MR imaging: techniques and acronyms. *Radiology*. 1993;186(1):1-8.

36. Merboldt K-D, Hänicke W, Gyngell ML, Frahm J, Bruhn H. The influence of flow and motion in MRI of diffusion using a modified CE-FAST sequence. *Magn Reson Med*. 1989;12(2):198-208.

37. Zur Y, Bosak E, Kaplan N. A new diffusion SSFP imaging technique. *Magn Reson Med*. 1997;37(5):716-722.

38. Miller KL, Meyer CM, Pauly JM. Self-navigated spirals for high resolution steady-state diffusion imaging. *Proc Int Soc Magn Reson Med*. 2002;10:1110.

39. Deoni SCL, Peters TM, Rutt BK. Quantitative diffusion imaging with steady-state free precession. *Magn Reson Med*. 2004;51(2):428-433.

40. Bieri O, Ganter C, Welsch GH, Trattnig S, Mamisch TC, Scheffler K. Fast diffusion-weighted steady state free precession imaging of in vivo knee cartilage. *Magn Reson Med*. 2012;67(3):691-700.

41. Weaver JB, Van Houten EEW, Miga MI, Kennedy FE, Paulsen KD. Magnetic resonance elastography using 3D gradient echo measurements of steady-state motion. *Med Phys*. 2001;28(8):1620-1628.

42. Zur Y, Stokar S, Bendel P. An analysis of fast imaging sequences with steady-state transverse magnetization refocusing. *Magn Reson Med*. 1988;6 (2):175-193.

43. Pelc NJ, Bernstein MA, Shimakawa A, Glover GH. Encoding strategies for three-direction phase-contrast MR imaging of flow. *J Magn Reson Imaging*. 1991;1(4):405-413.

44. McNab JA, Miller KL. Sensitivity of diffusion weighted steady state free precession to anisotropic diffusion. *Magn Reson Med*. 2008;60(2):405-413.

45. Stanford Body Magnetic Resonance Group. Extended Phase Graph Functions and Examples. https://web.stanford.edu/~bah/software/epg/. Accessed September 4, 2018.

46. Jiang Y, Ma D, Seiberlich N, Gulani V, Griswold MA. MR fingerprinting using fast imaging with steady state precession (FISP) with spiral readout. *Magn Reson Med*. 2015;74(6):1621-1631.

47. Stejskal EO, Tanner JE. Spin diffusion measurements: spin echoes in the presence of a time-dependent field gradient. *J Chem Phys*. 1965;42(1):288-292.

48. Basser PJ, Mattiello J, LeBihan D. MR diffusion tensor spectroscopy and imaging. *Biophys J*. 1994;66(1):259-267.

49. SNAPHU: Statistical-Cost, Network-Flow Algorithm for Phase Unwrapping. http://step.esa.int/main/third-party-plugins-2/snaphu/. Accessed September 4, 2018.

50. Chen CW, Zebker HA. Network approaches to two-dimensional phase unwrapping: intractability and two new algorithms. *J Opt Soc Am A*. 2000;17 (3):401.

51. Chen CW, Zebker HA. Two-dimensional phase unwrapping with use of statistical models for cost functions in nonlinear optimization. *J Opt Soc Am A*. 2001;18(2):338.

52. Chen CW, Zebker HA. Phase unwrapping for large SAR interferograms: statistical segmentation and generalized network models. *IEEE Trans Geosci Remote Sens*. 2002;40(8):1709-1719.

53. Fovargue D, Kozerke S, Sinkus R, Nordsletten D. Robust MR elastography stiffness quantification using a localized divergence free finite element reconstruction. *Med Image Anal*. 2018;44:126-142.

54. McGarry MDJ, Van Houten EEW, Perriñez PR, Pattison AJ, Weaver JB, Paulsen KD. An octahedral shear strain-based measure of SNR for 3D MR elastography. *Phys Med Biol*. 2011;56(13):N153-N164.

55. Aletras AH, Ding S, Balaban RS, Wen H. DENSE: displacement encoding with stimulated echoes in cardiac functional MRI. *J Magn Reson*. 1999;137 (1):247-252.

56. Glaser KJ, Felmlee JP, Manduca A, Ehman RL. Shear stiffness estimation using intravoxel phase dispersion in magnetic resonance elastography. *Magn Reson Med*. 2003;50(6):1256-1265.

57. Yin Z, Kearney SP, Magin RL, Klatt D. Concurrent 3D acquisition of diffusion tensor imaging and magnetic resonance elastography displacement data (DTI-MRE): theory and in vivo application. *Magn Reson Med*. 2017;77(1):273-284.

58. Malik SJ, Padormo F, Price AN, Hajnal JV. Spatially resolved extended phase graphs: modeling and design of multipulse sequences with parallel transmission. *Magn Reson Med*. 2012;68(5):1481-1494.

59. Weigel M, Schwenk S, Kiselev VG, Scheffler K, Hennig J. Extended phase graphs with anisotropic diffusion. *J Magn Reson*. 2010;205(2):276-285.

60. Scheffler K, Maderwald S, Ladd ME, Bieri O. Oscillating steady states. *Magn Reson Med*. 2006;55(3):598-603.

61. Assländer J, Glaser SJ, Hennig J. Pseudo steady-state free precession for MR-fingerprinting. *Magn Reson Med*. 2017;77(3):1151-1161.

62. Amthor T, Doneva M, Koken P, Sommer K, Meineke J, Börnert P. Magnetic resonance fingerprinting with short relaxation intervals. *Magn Reson Imaging*. 2017;41:22-28.

63. Talwalkar JA. Elastography for detecting hepatic fibrosis: options and considerations. *Gastroenterology*. 2008;135(1):299-302.

64. Yin M, Talwalkar JA, Glaser KJ, et al. Assessment of hepatic fibrosis with magnetic resonance elastography. *Clin Gastroenterol Hepatol*. 2007;5 (10):1207-1213.

65. Buehrer M, Curcic J, Boesiger P, Kozerke S. Prospective self-gating for simultaneous compensation of cardiac and respiratory motion. *Magn Reson Med*. 2008;60(3):683-690.

66. Patz S, Hawkes RC. The application of steady-state free precession to the study of very slow fluid flow. *Magn Reson Med*. 1986;3(1):140-145.

67. Larson AC, Kellman P, Arai A, et al. Preliminary investigation of respiratory self-gating for free-breathing segmented cine MRI. *Magn Reson Med*. 2005;53(1):159-168.

68. Lustig M, Donoho D, Pauly JM. Sparse MRI: the application of compressed sensing for rapid MR imaging. *Magn Reson Med*. 2007;58(6):1182-1195.

SUPPORTING INFORMATION

Additional supporting information may be found online in the Supporting Information section at the end of the article.

APPENDIX A

General MRE Propagator for a Trapezoidal Gradient Lobe

The motion propagator for a trapezoidal gradient with finite slope time t_d, duration T, and gradient area Δk is given by

$$\mathbf{J} = \exp\left\{\frac{-i\vec{r}_0 \cdot \Delta\vec{k}}{\omega^2 t_d(T-t_d)}\left(\sin(\phi) + (1+\omega^2 t_d(T-t_d))\sin(\omega T + \phi) - \sin(\phi + \omega t_d) - \sin(\phi + \omega(T-t_d)))\right)\right\}\mathbf{J}_0$$

The propagator in the absence of the gradient is equivalent to $\mathbf{J}_0$ in Eq. 19.

APPENDIX B

Definition of Motion Propagators for the Two-Transverse TR Approximation

To evaluate the two-transverse TR approximation, the motion propagators for storage and transverse magnetization periods need to be defined. The propagator directly preceeding readout is given by

$$\mathbf{J}_{T0} = \mathbf{J}|_{\to k_0 \to -\Delta \to k}.$$

Here, the notation $\bullet|_{rule}$ should be interpreted as a replacement rule, which is applied to the expression on its left.

The motion propagator directly following initial RF excitation is given by

$$\mathbf{J}_T(mT_R) = \left(\mathbf{J}|_{\vec{K}_0 \to 0, \, \phi \to \phi - \omega T_R(m+1)}\right) \cdot \left(\mathbf{J}_0|_{\vec{K}_0 \to \Delta\vec{K}, \, T \to T_R - T, \, \phi \to \phi - \omega T_R(m+1) + \omega T}\right).$$

The first term denotes initial sensitization through the unipolar MEG, while the second term accounts for phase accrual due to magnetization being spoiled.

Configuration states in longitudinal storage experience motion sensitization over the duration of the storage period mT_R. The motion propagator is thus given by

$$\mathbf{J}_L(mT_R) = \left(\mathbf{J}_0|_{\vec{K}_0 \to \Delta k^{\to}, \, T \to mT_R, \, \phi \to \phi - \omega T_R m}\right)$$

APPENDIX C

Derivation of the Two-Transverse TR Approximation in the Presence of Bulk Periodic Motion

For the derivation of the two-transverse TR approximation in the presence of periodic bulk motion, we follow McNab and Miller, Ref. [44] except for the respective additions for unipolar MRE. Each echo pathway is preceded by infinitely many longitudinal storage states, which have to be taken into account to capture T_1 recovery. These contributions are given by the factor

$$M_0(1-E_1)\sum_{n=0}^{\infty}(E_1\cos(\alpha))^n = M_0\frac{1-E_1}{1-E_1\cos(\alpha)}, \tag{35}$$

where M_0 is the equilibrium magnetization. The solution of the infinite series is given by the geometric series identity[69]

$$\sum_{n=0}^{\infty}r^m = \frac{1}{1-r}, \quad \text{with} \quad |r| < 1. \tag{36}$$

Since $k=0$ holds for these states, they are not subject to motion sensitization. Taking the remaining transverse periods and the RF pulses into account, the spin-echo contribution can be stated as

$$SE = -\frac{M_0(1-E_1)E_2\sin^2(\alpha/2)\sin(\alpha)}{1-E_1\cos(\alpha)}\cdot\mathbf{J}_T^*(T_R)\mathbf{J}_{T0}. \tag{37}$$

The stimulated echo (STE) contributions are given by two distinct terms. The STE contributions are given by (STE$_1$: one storage period)

$$STE_1 = -\frac{M_0(1-E_1)E_1E_2\sin^3(\alpha)}{2(1-E_1\cos(\alpha))}\cdot \mathbf{J}_T^*(2T_R)\mathbf{J}_L^*(T_R)\mathbf{J}_{T0}. \tag{38}$$

and (m>1 longitudinal storage periods)

$$STE_{m>1} = -\frac{M_0(1-E_1)E_2\sin^3(\alpha)}{2\cos(\alpha)(1-E_1\cos(\alpha))}(E_1\cos(\alpha))^m\cdot \mathbf{J}_T^*((m+1)T_R)\mathbf{J}_L^*(mT_R)\mathbf{J}_{T0}. \tag{39}$$

The steady-state echo is given by a superposition of these terms, yielding

$$S = SE + STE_1 + \sum_{m=2}^{\infty} STE_m. \tag{40}$$

Insertion of the STE definition into the infinite sum leads to

$$\sum_{m=2}^{\infty} STE_m = -\frac{M_0(1-E_1)E_2\sin^3(\alpha)}{2\cos(\alpha)(1-E_1\cos(\alpha))}\mathbf{J}_{T0}\underbrace{\sum_{m=2}^{\infty}(E_1\cos(\alpha))^m\cdot \mathbf{J}_T^*((m+1)T_R)\mathbf{J}_L^*(mT_R)}_{=A}. \tag{41}$$

An auxiliary term A can be identified by collecting all terms dependent on m. Shifting the summation index $m \to m-2$, we arrive at

$$A = (E_1\cos(\alpha))^2 \sum_{m=0}^{\infty}(E_1\cos(\alpha))^m\cdot \mathbf{J}_T^*((m+3)T_R)\mathbf{J}_L^*((m+2)T_R). \tag{42}$$

Splitting the infinite sum into two

$$A = (E_1\cos(\alpha))^2 \sum_{m=0}^{\infty}\sum_{n=0}^{N_P-1}(E_1\cos(\alpha))^{mN_P+n}\cdot \mathbf{J}_T^*((mN_P+n+3)T_R)\mathbf{J}_L^*((mN_P+n+2)T_R)$$

allows to make use of the periodicity of the motion propagators implied by the Ristretto sequence timing, i.e.

$$\mathbf{J}_T((m+N_P)T_R) = \mathbf{J}_T(mT_R).$$

$$\mathbf{J}_L((m+N_P)T_R) = \mathbf{J}_L(mT_R).$$

simplifying the STE contributions to

$$A = \left(\sum_{m=0}^{\infty}(E_1\cos(\alpha))^{2+mN_P}\right)\underbrace{\left(\sum_{n=0}^{N_P-1}(E_1\cos(\alpha))^n\cdot \mathbf{J}_T^*((n+3)T_R)\mathbf{J}_L^*((n+2)T_R)\right)}_{=\kappa(N_P)}. \tag{43}$$

The summation over m can again be performed, leading to

$$A = \frac{(E_1\cos(\alpha))^2}{1-(E_1\cos(\alpha))^{N_P}}\kappa(N_P). \tag{44}$$

Hence, the STE contributions with $m > 1$ are given by

$$\sum_{m=2}^{\infty} STE_m = -\frac{M_0(1-E_1)E_1^2E_2\sin^3(\alpha)\cos(\alpha)}{2(1-E_1\cos(\alpha))}\frac{\kappa(N_P)\mathbf{J}_{T0}}{1-(E_1\cos(\alpha))^{N_P}}. \tag{45}$$